Lab on a Chip

ROYAL SOCIETY OF CHEMISTRY

CRITICAL REVIEW

View Article Online
View Journal

Cite this: DOI: 10.1039/d5lc00864f

Yield stress fluids in microfluidics: research, applications and opportunities

Hossein Rahmani [a] and Seyed Mohammad Taghavi *[b]

Microfluidic technology enables scalable solutions in precision medicine, diagnostics, drug delivery, organ-on-a-chip models, single-cell analysis, high-throughput screening, and environmental monitoring. In fact, many of these applications process fluids with complex rheology, *e.g.*, blood, mucus, bioinks, and polymer or particle suspensions, exhibiting yield stress, viscoelasticity, and shear-thinning that govern transport, mixing, and interfacial dynamics at small scales. However, the interplay of such rheology with microscale confinement, roughness, and surface patterning remains underexplored. In this review, we highlight microfluidic applications where yield stress (and related rheological) properties are pivotal. For instance, we discuss how blood rheology shapes the design of devices for circulating tumor cell separation, and how bioink viscoelasticity balances flowability and shape fidelity in extrusion and embedded bioprinting. We also examine electrorheological fluids as field-tunable media for microvalves, pumps, and mixers, and analyze microorganism and microrobot locomotion in complex fluids, linking physics to biology and targeted delivery. We further consider microscale slip, microrheology platforms, and viscous fingering instabilities, to specifically highlight how rheology controls transport and enables fabrication of channels and hydrogel structures. We conclude that yield-stress (and viscoelastic) effects are not mere complications but they are powerful design variables, and we outline future opportunities for leveraging these properties to advance microfluidic science and technology.

Received 10th September 2025,
Accepted 16th March 2026

DOI: 10.1039/d5lc00864f

rsc.li/loc

[a] *Department of Mathematics, The University of British Columbia, Vancouver, Canada. E-mail: hossein.rahmani@ubc.ca*
[b] *Department of Chemical Engineering, Universite Laval, Quebec, Canada. E-mail: seyed-mohammad.taghavi@gch.ulaval.ca*

1 Introduction

Microfluidic technology enables precise fluid handling and manipulation at sub-millimetre scales, allowing parallel

Hossein Rahmani

Dr. Hossein Rahmani is a Banting Postdoctoral Fellow at the University of British Columbia. He studied mechanical engineering at the bachelor's and master's levels and completed a Ph.D. in Chemical Engineering at Université Laval, Quebec, Canada. His doctoral work focused on developing mathematical and computational models for viscoplastic flows over superhydrophobic surfaces. Since December 2023, his postdoctoral research at UBC has centered on modeling viscoplastic and elasto-viscoplastic flows, with applications in energy, environmental, and biomedical engineering. His work has been recognized with distinctions including the Banting Fellowship and the ACS Rising Star in Chemical Engineering award.

Seyed Mohammad Taghavi

Dr. Seyed Mohammad Taghavi is a Canada Research Chair in Modeling Complex Flows and Full Professor in the Department of Chemical Engineering at Université Laval (since 2014). He received his Ph.D. from the University of British Columbia in 2011 and subsequently held Banting and Tomlinson postdoctoral fellowships at the University of Michigan and McGill University. His research focuses on complex and interfacial flows, hydrodynamic instabilities, and non-Newtonian fluid mechanics. His work has been recognized with distinctions including a Humboldt Fellowship for Experienced Researchers and the ACS Class of Influential Researchers award.

experiments with minimal sample volumes. It can span applications in medicine, chemistry, biology, and engineering,[1] and has indeed transformed diagnostics, drug discovery, chemical synthesis, and energy conversion.[2,3] In these devices, surface forces typically dominate over volumetric forces, and laminar dynamics allow effective flow control; this enables advanced functionalities, *e.g.*, rapid diffusive mixing and efficient heat and mass transfer.[4] Microfluidics is generally classified as continuous-flow or droplet-based, and continuous-flow systems are particularly suited to precise reagent delivery, continuous particle and cell separation, complex reaction sequences, and integrated sensing.[5,6] Droplet microfluidics manipulates discrete pico–nano litre volumes within an immiscible carrier fluid, creating isolated microreactors for high-throughput screening, single-cell analysis, and the synthesis of monodisperse particles.[7] In many of such applications, the processed fluids exhibit complex non-Newtonian rheology, which critically affects device performance. Accordingly, rheological considerations are central to microfluidic design/optimisation. In this context, our review surveys microfluidic applications where rheology is decisive, with emphasis on yield-stress materials. While these have been extensively studied in macroscopic systems (see, *e.g.*, Table 1), their importance is now increasingly recognized at the microscale, and this motivates the present review.

Yield-stress materials are non-Newtonian materials that can sustain finite shear stresses without macroscopic flow on the timescale of observation. Below a threshold called yield stress they respond in a solid-like manner (typically elastic/viscoelastic, sometimes with slow creep), whereas above this threshold they undergo irreversible deformation and flow like a viscous fluid. In ideal viscoplastic models (*e.g.*, Bingham/Herschel–Bulkley), the strain rate is zero for stresses below the yield stress.[8,9] A familiar every day example may be toothpaste, which requires sufficient force to extrude. Yield-stress behaviour is observed across materials, *e.g.*, from waxy crude oil to foods, cosmetics, and pharmaceuticals (*e.g.*, chocolate cream, jam, moisturising cream, hair gel, ointments, medicinal syrups),[8,9] and it is also characteristic of many biological fluids, including blood, mucus, and other biofluids[10–12] (see Fig. 1). Beyond yielding, such materials may also exhibit shear-thinning/thickening, elasticity, or thixotropy.[13,14] In shear-thinning (pseudoplastic) fluids, viscosity decreases with shear rate, whereas in shear-thickening (dilatant) fluids, it increases.[15] Yield-stress fluids with predominantly viscous and plastic behaviour are often termed viscoplastic.[13] Elasticity arises when a fluid subjected to rapid strain deforms but partially recovers once the strain is removed, in contrast to purely viscous fluids that dissipate energy as heat. This behaviour stems from microstructure, where entangled polymer chains stretch and recoil like springs, storing elastic energy.[16] Thus, viscoelastic fluids display memory effects and are characterised by normal stress differences, central to their dynamics.[17] Finally, thixotropy denotes time-dependent shear-thinning, in which viscosity typically decreases progressively under constant shear due to microstructural breakdown, followed by recovery upon rest.[18] As explained in Larson *et al.*,[14] in both viscoelastic and thixotropic fluids, the stresses depend on their past deformation history. However, the difference is that viscoelastic fluids are characterized by elasticity, while

Table 1 Selected review articles on yield stress fluids and their relevance to the current work

References	Focus and key contributions	Relevance to current review
Balmforth *et al.* (2014)[8]	Comprehensive review of viscoplastic fluid mechanics, emphasizing modeling, flow behavior, and analytical challenges posed by yield stress	Establishes theoretical foundations for interpreting yield-stress behavior in complex and confined geometries
Bonn *et al.* (2017)[9]	Review of yield stress materials in soft matter, linking microscopic structure to nonlinear flow and highlighting shear banding, wall slip, and nonlocality	Clarifies microstructural origins of yielding and flow heterogeneity in confined soft materials
Coussot (2014)[39]	Experimental review of yield stress fluid flows across diverse geometries, emphasizing transitions between solid-like and liquid-like behavior	Reveals challenges in interpreting flow fields and boundary effects in confined viscoplastic systems
de Souza Mendes (2012)[40]	Review of thixotropy models for yield stress fluids with elasticity, comparing algebraic and differential formulations and structural evolution dynamics	Informs the selection and interpretation of constitutive models in time-dependent microrheological flows
Ewoldt & McKinley (2017)[41]	Proposes multidimensional Pipkin maps to organize thixotropic, elastic, and viscoplastic responses under complex flow protocols	Provides conceptual framework for classifying transient and nonlinear microrheological behavior in thixotropic elastoviscoplastic materials
Fraggedakis *et al.* (2016)[42]	Comparative evaluation of elasto-visco-plastic models in rheometric and complex flows	Guides model selection for predicting microrheological responses in shear-thinning, confined, or unsteady viscoplastic flows
Frigaard (2019)[43]	Defense and critique of simple viscoplastic models	Contextualizes use of idealized models in complex fluids
Piau (2007)[44]	Detailed structural and rheological analysis of Carbopol gels, including elastoplasticity, wall slip, and scaling laws for concentration-dependent behavior	Provides benchmark insights into soft glassy rheology and interfacial effects central to microrheological measurements
Saramito & Wachs (2017)[45]	Review of numerical strategies for simulating viscoplastic flows, including recent advances and applications involving slip, thixotropy, and multiphase systems	Supports the development of accurate computational tools for modeling confined and complex microrheological flows

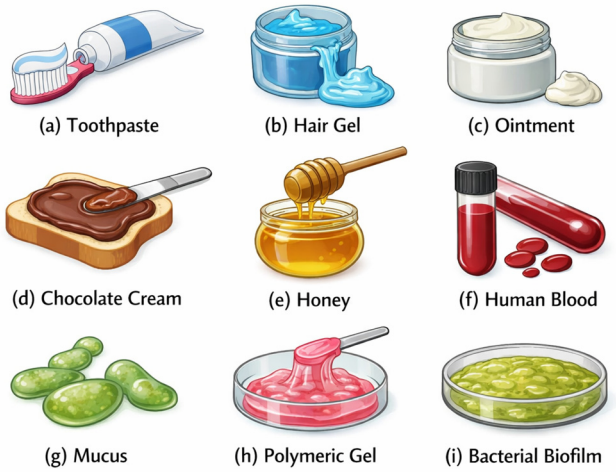

Fig. 1 Examples of yield stress fluids.

the viscosity (or yield stress) of thixotropic materials shows slow time-dependent variations. In other words, in viscoelastic materials, long polymers deform elastically without breaking, causing viscoelastic behavior. However, thixotropy appears due to particle clusters connected by inextensible, fragile, bonds that can break reversibly under stress, leading to a temporary reduction in viscosity with insignificant storage of elastic energy. Ovarlez *et al.*[19] demonstrated a distinct flow response beyond simple and thixotropic yield-stress rheology, which they termed the rheopectic yield-stress behavior. The rheopexy of the yield-stress fluid was illustrated through rheological tests on carbon black suspensions, in which a viscosity-bifurcation phenomenon around a critical stress was observed. Notably, after a pre-shear at a prescribed stress, the material accelerated when a lower stress was subsequently imposed. Rheopexy can be as important as thixotropy when working with yield-stress fluids in microfluidic environments. We should also highlight that thixotropy and rheopexy are closely related, as they represent opposite manifestations of time-dependent rheological behavior.

Interestingly, yield-stress values have been measured in various biofluids, including human blood, serum albumin solutions, and mucus.[8,11,20] Globular proteins, *e.g.*, serum albumins, *i.e.*, key components of mammalian blood that shape biofluid microstructure, induce yield-stress-like responses across concentrations.[11,12,21,22] Consequently, blood exhibits "measurable" yield stress, which is essential to its physiological functions.[11,20] These proteins are also central to foods, pharmaceuticals, and cosmetics.[11] The yield-stress and shear-thinning behaviour of blood arise from red blood cell interactions forming three-dimensional *rouleaux* networks at low shear, while its viscoelasticity stems from elastic deformation of individual cells at high shear.[23,24] Rouleaux formation is explained based on a competition between short-range attractive interactions enhanced by plasma macromolecules (*e.g.* fibrinogen) and electrostatic/hydration repulsion at the red blood cell surface. Different factors including the suspension medium composition, the elasticity of red blood cell membranes, the hematocrit of blood and the applied shear rate affect the rouleaux formation.[25] Rouleaux networks are largely reversible: aggregates formed at low shear disperse under sufficiently strong shear stress and can re-form as the stress is reduced.[26] As shown in Fig. 2, with decrease in blood flow rate, larger rouleaux networks are formed, highlighting the role of shear rate in rouleaux formation.[25] Furthermore, the attractive interactions between the blood constituents, together with the low shear, may promote the formation of vorticity-aligned structures.[27]

Mucus, *i.e.*, a viscoelastic gel also with measurable yield stress, forms a protective epithelial barrier,[28,29] providing lubrication, pathogen entrapment, and mucociliary clearance.[28,30] Composed primarily of mucin glycoproteins, water, and macromolecules, the rheology of mucus is altered in diseases, *e.g.*, cystic fibrosis or chronic bronchitis, where elevated yield stress and elasticity impair clearance, compromise organ function, and heighten infection risk.[28,31]

Microbial biofilms are communities of microorganisms embedded in a self-produced extracellular polymeric substance (EPS) matrix, whose rheology governs structural integrity, ecological persistence, and resistance to external stresses.[32,33] Biofilms often exhibit viscoelasticity with a finite yield stress.[34,35] Their intrinsic composition and microstructure (*e.g.*, EPS chemistry, crosslinking, cell density, and hydration) set key material parameters such as the elastic/viscous moduli, characteristic relaxation times, and the magnitude of the yield stress. For a given composition, the observed mechanical response depends on external loading: biofilms behave as soft solids under stresses below the yield threshold and/or on timescales shorter than dominant relaxation processes, but they can creep, reorganize, and flow as viscoelastic fluids when stresses approach or exceed the yield stress and when deformation is

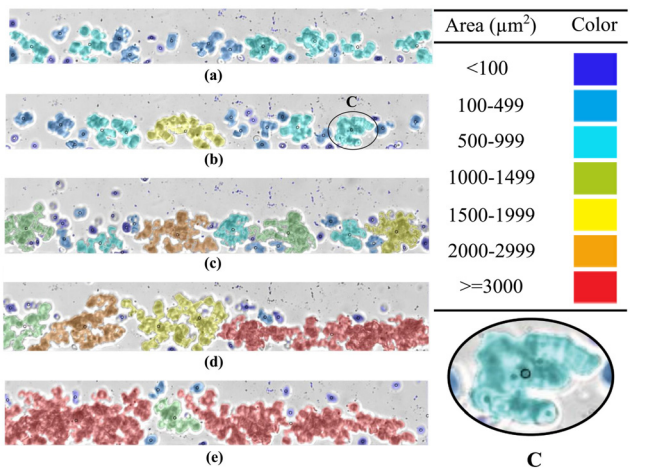

Fig. 2 Images of human red blood cell aggregates adapted from ref. 25. At 10% hematocrit, from (a) to (e), the flow rate decreases as 35, 20, 10, 7.5 and 5 μL h^{-1}, respectively. The coloring is based on the aggregate size. The highlighted region C shows a rouleaux.

applied over sufficiently long timescales. This arises from the hydrated EPS network of polysaccharides, proteins, and extracellular DNA, which provides mechanical stability while permitting elastic recovery and viscous flow.[36] In particular, these properties enable biofilms to withstand shear forces, resist mechanical cleaning and immune responses, and facilitate nutrient transport and intercellular signalling.[33,37] Their stiffness and elasticity underpin adhesion and persistence, which drive industrial biofouling (*e.g.*, pipelines) and chronic medical infections (*e.g.*, implants).[32,38]

In this review, we examine applications in which yield-stress rheology is central to microfluidic technology, as schematically presented in Fig. 3. First, we introduce models developed for yield-stress fluids, with emphasis on viscoplastic materials. We then discuss microfluidic platforms, their applications, and methods for flow handling and droplet manipulation, illustrated with specific examples. Finally, we critically assess cases where yield-stress fluids can be used/manipulated within microdevices, emphasising the importance of non-Newtonian rheology, and also outline research directions where such yield-stress effects may strongly influence microfluidic flow dynamics.

2 Yield stress rheology

A fundamental tool to better understand non-Newtonian behaviour is the flow curve, which plots shear stress against shear rate (see Fig. 4). We note that the flow curve corresponds to a steady-state response and, as such, does not capture transient dynamics. Therefore, since transient flows can be long-lived (particularly in confined geometries), the steady flow curve may provide limited guidance, and should be complemented by time-dependent tests such as start-up shear (stress-growth), creep and recovery, stress relaxation, and rate- or stress-step protocols that directly resolve transient dynamics. Considering the flow curve, the ratio of stress to shear rate defines the effective viscosity, which forms the basis of the generalized Newtonian fluid model, *i.e.*, widely used in engineering for its simplicity and the accessibility of rheometric data.[46] In this section, we introduce the principal constitutive equations for yield-stress rheology, focusing on viscoplastic models (Bingham, Herschel–Bulkley, Casson) and briefly discussing the a well-known elasto-viscoplastic model (*i.e.*, the Saramito model).

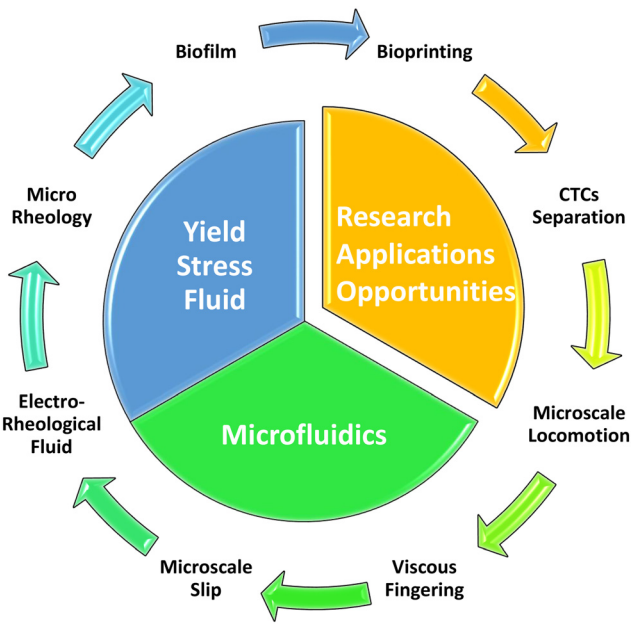

Fig. 3 Representative schematic of the topics covered in this review.

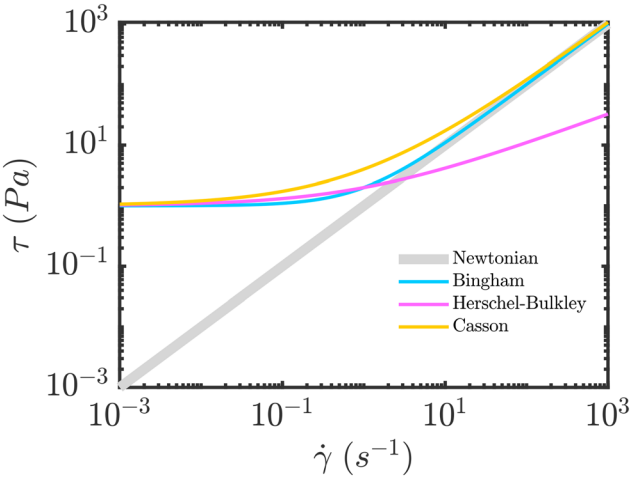

Fig. 4 Schematic curves showing the stress *versus* strain-rate variation for different rheological models.

2.1 Constitutive equations

2.1.1 Bingham model. Bingham constitutive equation is the simplest model used to describe the yield stress rheology:

$$\begin{cases} \underline{\underline{\tau}} = \left(\mu_p + \dfrac{\tau_0}{\dot{\gamma}}\right)\underline{\underline{\dot{\gamma}}}, & \tau > \tau_0, \\ \underline{\underline{\dot{\gamma}}} = 0, & \tau \le \tau_0, \end{cases} \tag{1}$$

where τ_0 is the fluid yield stress and μ_p represents the plastic viscosity. In addition, $\underline{\underline{\tau}}$ is the stress tensor and $\underline{\underline{\dot{\gamma}}} = \nabla \boldsymbol{u} + (\nabla \boldsymbol{u})^T$ represents the strain rate tensor, while $\tau = \sqrt{\tau_{ij}\tau_{ij}/2}$ and $\dot{\gamma} = \sqrt{\dot{\gamma}_{ij}\dot{\gamma}_{ij}/2}$ are the norms of the stress and strain rate tensors, respectively. As described in eqn (1) and illustrated in Fig. 4, the yield stress fluid shows a viscous-like deformation when the stress is larger than yield stress; otherwise, no deformation of the material is considered.

In yield stress fluids problems, the Bingham number (denoted typically with Bi or alternatively B) is a key dimensionless parameter representing the ratio of the yield stress (τ_0) to a characteristic viscous stress (τ_{ch}):

$$\mathrm{Bi} = \frac{\tau_0 H_0}{\mu_p U_0}, \tag{2}$$

where U_0 and H_0 are the characteristic velocity and length scale, respectively, and μ_p is the plastic viscosity. Depending on the flow dynamics under interest and thus the definition of the characteristic stress, other dimensionless parameters, *e.g.*, the yield number,[47,48] have been also introduced, comparing the material yield stress to a relevant driving stress scale such as buoyancy, inertial, or viscous stresses. Other dimensionless numbers may also be relevant depending on the system under consideration; for example, the Mason number, which compares hydrodynamic shear to inter-particle adhesion, plays an important role in gel dynamics.[49,50]

2.1.2 Herschel–Bulkley model. The Herschel–Bulkley constitutive equation is a widely used model that can address the yield stress, and shear thinning/thickening behaviors:[46]

$$\begin{cases} \underline{\underline{\tau}} = \left(k\dot{\gamma}^{n-1} + \dfrac{\tau_0}{\dot{\gamma}} \right) \underline{\underline{\dot{\gamma}}}, & \tau > \tau_0, \\ \underline{\underline{\dot{\gamma}}} = 0, & \tau \le \tau_0, \end{cases} \tag{3}$$

where k is the consistency coefficient, and n represents the power law exponent. The Herschel–Bulkley model generally fits well on the rheometric data.[8] In addition, at large strain-rates, this model converges to a power-law model with shear-thinning/thickening rheology (see Fig. 4).

2.1.3 Casson model. Casson model is mostly used in studying specific yield stress fluids, such as blood. Based on the Casson model,[51] the shear stress (τ) is described as:

$$\begin{cases} \sqrt{\underline{\underline{\tau}}} = \sqrt{\tau_0} + \sqrt{\mu \underline{\underline{\dot{\gamma}}}}, & \tau > \tau_0, \\ \underline{\underline{\dot{\gamma}}} = 0, & \tau \le \tau_0, \end{cases} \tag{4}$$

where μ is the viscosity.

The Casson model was proven to be the most suitable constitutive equation to describe the blood rheology in steady state shear condition. Based on the steady-state blood flow experiments, the following has been revealed: (1) blood exhibits yield stress values.[52,53] (2) The yield stress value is correlated with the concentration of plasma fibrinogen, *i.e.*, an elongated plasma protein that plays a crucial role in blood clotting.[54,55] (3) There is a critical hematocrit, *i.e.*, a threshold concentration of red blood cells in the blood, to exhibit a yield stress.[56] (4) There is a transition from non-Newtonian to Newtonian flow in high shear rates[57] (see Fig. 4).

2.1.4 Saramito model. Saramito[67] introduced a new constitutive equation to model the elasto-viscoplastic fluids through combining the Oldroyd-B and Bingham models. The Oldroyd-B model is a widely used constitutive equation to model the behavior of viscoelastic fluids[68,69] and the Bingham model is the simplest yield stress model that only considers the yield stress threshold. Therefore, the Saramito model is described as:[67]

$$\lambda \overset{\triangledown}{\underline{\underline{\tau}}} + \max\left(0, 1 - \frac{\tau_0}{\|\tau\|_v}\right) \underline{\underline{\tau}} - \mu_p \underline{\underline{\dot{\gamma}}} = 0, \tag{5}$$

where λ is the relaxation time. $\|\tau\|_v = \sqrt{\frac{1}{2}\tau_{ij}\tau_{ij}}$ is the von Mises equivalent stress used in the yield criterion: the material yields when $\|\tau\|_v$ exceeds the yield stress τ_0. For $\|\tau\|_v > \tau_0$, the material flows with a viscous-like (plastic) deformation, whereas for $\|\tau\|_v < \tau_0$, it remains unyielded and can sustain only elastic strain (no plastic flow).[67,70] The Cauchy stress tensor represents the total stress acting on a fluid element, including the isotropic pressure contribution. For elasto-viscoplastic materials, the Caushy stress tensor is defined as $\underline{\underline{\sigma}} = -p\underline{\underline{I}} + \underline{\underline{\tau}} + \mu_s \underline{\underline{\dot{\gamma}}}$, where $\underline{\underline{I}}$ is the unit tensor and μ_s is the solvent viscosity ($\mu_s\dot{\gamma}$ represents the solvent contribution to the total stress). The downward triangle on top of the stress tensor in eqn (5) represents the upper-convected derivative.[67,70]

In addition to the widely used models described above for yield-stress materials, more recent frameworks; including the TC[71] and KDR[72] models, have been developed, each with distinct advantages and limitations. For instance, the TC model was developed to describe the flow curve of soft glassy, yield-stress materials by explicitly separating elastic, plastic, and viscous dissipation mechanisms. Conceptually, the model predicts three regimes: solid-like/yield-dominated response at low shear rate, an intermediate plastic regime, and a high-viscous regime where the stress approaches linear scaling; thus improving the physical interpretability of the model parameters. On the other hand, the KDR model unifies the physics above and below the yield stress by introducing a rate-dependent relaxation time that allows for plastic deformation below the yield stress. The model also demonstrates that yielding is promoted by a rapid elastic deformation. Despite their mechanistic appeal, these more recent constitutive frameworks (*e.g.*, KDR, and TC) have only rarely been adopted in microfluidics studies to date,[73,74] where simplified yield-stress fits (*e.g.*, Bingham or Herschel–Bulkley laws) remain the dominant modeling choice.

While constitutive models provide a formal definition of a yield stress, its experimental determination is more nuanced and depends on which yielding is being probed. In practice, one often distinguishes (i) a static yield stress associated with the solid-to-liquid transition, inferred from protocols such as start-up shear, creep, or strain sweeps, and (ii) a dynamic yield stress associated with the liquid-to-solid transition, commonly obtained by extrapolating the steady flow curve as $\dot{\gamma} \to 0$. Because these two measures have different physical origins and remain sensitive to protocol, geometry, and sample history, reported yield stress values can vary widely.[9] Table 2 summarizes challenges identified in recent rheological studies and highlights their specific implications

Table 2 Challenges in measuring yield stress identified in recent studies and their relevance to microfluidic flows

References	Identified challenges	Potential relevance to microfluidic flows
Møller *et al.* (2006)[58]	Yield stress measurements are highly protocol-dependent due to thixotropy; the yield stress is not intrinsic but history-dependent	Undermines the use of a single yield stress value in microfluidic experiments where flow history and confinement strongly affect material response
Moller *et al.* (2009)[59]	Yield stress ambiguity arises from conflating thixotropic and simple yield stress fluids; resolving this distinction enables reproducible measurements	Highlights the need to account for time-dependent structure (aging, rejuvenation) in confined microflows where shear history and spatial heterogeneity dominate
Ovarlez *et al.* (2013)[19]	Standard Herschel–Bulkley models often fail due to shear banding and nonlocal effects; careful protocols and geometry selection are critical	Underscores the limitations of macroscopic rheological models in confined systems and motivates incorporating nonlocality in microfluidic analyses
Divoux *et al.* (2024)[60]	Lack of unified understanding of the yielding transition in soft amorphous solids; open questions span experimental, theoretical, and numerical domains	Highlights fundamental gaps in modeling and interpreting yielding in confined geometries, directly relevant to microfluidic applications involving soft matter
Larsson *et al.* (2013)[61]	Yield stress measurements lack universality; results depend strongly on technique and testing conditions	Emphasizes the importance of standardized and careful rheometric protocols when characterizing yield stress in microscale systems
Dinkgreve *et al.* (2016)[62]	Yield stress and strain values vary significantly depending on the measurement method, even for simple yield stress fluids; many criteria rely on arbitrary crossover definitions	Underscores the necessity of consistent, carefully chosen protocols when interpreting microrheological or confined flow measurements involving yield stress materials
Dhar *et al.* (2024)[63]	Yield stress measurements vary drastically across geometries due to shear banding, sedimentation, and structural heterogeneity in cement pastes	Highlights how flow inhomogeneities and particle migration in confined geometries can compromise rheological interpretations, *i.e.*, critical for microfluidic yield-stress fluid applications
Kavishvar *et al.* (2023)[64]	Mucus exhibits complex, disease-sensitive yield stress behavior that varies with composition and scale; measurement depends critically on macro *vs.* micro-rheological methods	Demonstrates the importance of microscale yield stress rheology in physiologically relevant confined geometries, *i.e.*, highly pertinent to diagnostics, drug delivery, and microfluidic modeling of biofluids
Kavishvar *et al.* (2024)[65]	Accurate measurement of very low yield stress is difficult with conventional rheometry due to sensitivity and resolution limits	Introduces a microfluidic extensional flow device enabling sub-Pa yield stress measurement *via* unyielded zone tracking, *i.e.*, ideal for confined geometries and biofluids relevant to microfluidics
De Kee *et al.* (2021)[66]	Persistent difficulties in reliably measuring very low yield stresses, especially in biofluids like blood; limitations of existing models and experimental protocols	Underscores the importance of accurate low yield stress measurements in soft biological fluids commonly encountered in microfluidic applications

for microfluidic flows. These issues highlight that microfluidic systems, with strong confinement and complex shear histories, are particularly sensitive to ambiguities in defining τ_y.

3 Microfluidic technology

Microfluidic technology has revolutionised fluid handling at the microscale, with applications across chemistry, biology, medicine, and the physical sciences.[1] Indeed, its impact is closely linked to lab-on-chip (LOC) devices, which have transformed experimental practice in chemistry and biology much as integrated circuits advanced computation. LOCs, which incorporate active or passive elements (*e.g.*, filters, valves, and mixers) enable complex biological, chemical, or physical experiments to be integrated on a single chip. Their ability to manipulate minute fluid volumes permits analyses with minimal sample quantities, *i.e.*, an advantage in biomedical applications, where less invasive procedures and diagnostics in resource-limited settings are facilitated. Moreover, reduced reagent use substantially decreases waste, which enhance environmental sustainability.[75]

Early detection of disease biomarkers is critical in combating pathogens, such as tumours and viruses (*e.g.*, COVID-19). Microfluidic technology enables highly accurate, rapid, and parallel diagnostics.[76] For example, polymerase chain reaction, *i.e.*, one of the most precise methods for detecting pathogen RNA, has been implemented in digital microfluidic systems,[77] while circulating tumour cells have been identified in peripheral blood using microfluidic devices.[10] Digital platforms have also actuated glucose assays in serum, saliva, plasma, and urine.[78] Beyond diagnostics, microfluidics are also used in drug development and testing, with organ-on-chip systems replicating physiological functions for tissue engineering and pharmacological studies.[79] In therapeutic applications, micromagnetic–microfluidic devices have been used to cleanse the blood of sepsis patients infected with *Candida albicans* fungi.[80]

In this section, we introduce different microfluidic technologies, while in section 4 we discuss in detail the significance of fluid rheology across different technologies and applications.

3.1 Continues-flow microfluidic technology

Continuous-flow microfluidics, *i.e.*, characterized by laminar fluid motion in microchannels and microtubes, offers a highly controlled platform for manipulating and synthesizing biological fluids and related materials.[2,3] At the microscale, this control arises from steady laminar flow and the high

surface-to-volume ratio.[4] In fact, such systems have been widely employed for nanoparticle synthesis in drug delivery, where steady-state operation enables precise control of particle size, morphology, and monodispersity.[81] Among applications involving micro- and nanoparticles, an especially important case is the separation of circulating tumour cells (CTCs) from cancer patient blood. In what follows, we examine methods developed for CTC separation as a means of illustrating the broader principles of continuous-flow microfluidic technology. Our aim here is to overview the main methods and phenomena underpinning device development, while we note that detailed explanations and exhaustive coverage of all approaches lie beyond the scope of this review.

3.1.1 An example application: separation of circulating tumor cells. Metastasis, which causes ~90% of cancer-related deaths, proceeds as CTCs detach from the primary tumour, enter the bloodstream, and establish secondary tumours in distant organs.[10,93] With cancer deaths projected to exceed 20 million annually by 2030,[10] early CTC detection is critical for diagnosis, prognosis, and therapy development.[10,93]

Microfluidic systems exploit physical properties such as size, deformability, density, and electric charge to isolate CTCs in a label-free, minimally invasive manner.[1] In filtration methods, filters with 6–10 μm pores separate CTCs by size,[1,94] while lateral filter arrays embed pores along the flow to reduce clogging[82] (Fig. 5a). Weir-based microstructures and resettable traps further improve capture and resistance to clogging[83,95] (Fig. 5b).

Hydrodynamic methods use inertial forces to focus cells by size for high-throughput sorting,[1] or deterministic lateral displacement (DLD) with post arrays[84] (Fig. 5c). Triangular micropillars enhance efficiency *via* prolonged contact with immunocoated surfaces[1,96] (Fig. 5d). Dean flow fractionation employs centrifugal vortices in spiral channels,[1] with spiral designs improving speed and purity[86,97] and double spirals increasing throughput[98,99] (Fig. 5e and f). Vortex chips capture larger CTCs in vortices formed by channel expansions, while smaller cells remain in flow[100,101] (Fig. 5g). Although the aforementioned methods may share similar inertial effects, each relies on a specific mechanism that is distinct from the others. For example, in deterministic lateral displacement, a balance of lateral forces determines how CTCs are displaced and sorted along a straight channel. In contrast, Dean-flow fractionation employs a spiral duct or channel specifically to exploit curvature-induced secondary (Dean) vortices and associated lift forces to focus and separate CTCs. Consequently, in designing a microfluidic CTC-sorting device (or each stage for a multi-stage device), one typically selects and optimizes a single dominant mechanism, while accounting for any secondary inertial effects. Beyond single-mechanism inertial microfluidic platforms, a growing class of hybrid CTC devices deliberately cascades distinct hydrodynamic modules (*e.g.*, Dean-focusing spirals, deterministic lateral displacement arrays, and vortex-reservoir traps) to improve purity at clinically relevant throughputs while preserving cell viability. A representative strategy is two-stage inertial-DLD sorting, where a spiral inertial pre-enrichment removes the bulk of blood cells and a downstream DLD stage provides flow-rate-insensitive, high-resolution size discrimination for rare tumor-cell isolation.[102,103] Related cascaded inertial designs similarly combine multiple curved/structured sections to superimpose lift, Dean drag, and centrifugal effects (*e.g.*, sequential spirals and a zigzag segment), thereby sharpening focusing/partitioning and enabling simultaneous recovery of multiple tumor-cell populations from blood.[104]

In dielectrophoresis, differences in dielectric properties separate CTCs from normal cells. Continuous-flow dielectrophoresis field-flow fractionation directs CTCs *via* combined electric, gravitational, and hydrodynamic forces[89] (Fig. 5h and i), with zone-based designs enhancing efficiency.[90] Finally, acoustic methods employ ultrasound-induced acoustophoresis, using radiation and impedance contrast forces to isolate CTCs label-free[92,105–107] (Fig. 5j and k).

3.2 Droplet microfluidics

Droplet-based microfluidics, *i.e.*, a key subcategory of microfluidic technologies,[3,115] involves generating and manipulating discrete droplets in immiscible phases. Operating at low Reynolds numbers, these systems exhibit laminar flows,[112] *i.e.*, a feature exploited in continuous-flow devices for precise control of concentration gradients.[4,116] While continuous-flow approaches scale poorly, since device size increases linearly with experiment number, droplet microfluidics provides a compact, high-throughput alternative, producing thousands of uniform, independently controllable microreactors per second.[112,117,118]

Micro-droplets offer high surface-area-to-volume ratios, which enable faster reaction kinetics and efficient mass transport. Example applications include logic operations,[119] drug delivery, biosensing, biomolecule synthesis, and diagnostics.[112] Recent advances have further enabled complex structures such as double emulsions,[120] microbubbles,[121] and hollow microcapsules.[109]

Droplet size and uniformity depend on channel geometry, interfacial tension, surface wettability, and viscosity contrast between dispersed and continuous phases. Their behaviour is governed by the capillary number, $Ca = \mu u/\gamma$, where μ and u are the viscosity and velocity of the continuous phase and γ the interfacial tension; a critical Ca threshold determines droplet pinch-off.[112]

Multiple platforms exist for droplet generation, each exploiting distinct mechanisms. In T-junctions, the dispersed phase enters perpendicularly into the continuous stream, with shear and pressure gradients driving break-off[108,122] (Fig. 6). Flow-focusing geometries confine fluids through narrow orifices, producing symmetric shear fields for uniform droplets[123,124] (Fig. 7). Electric-field-based methods,

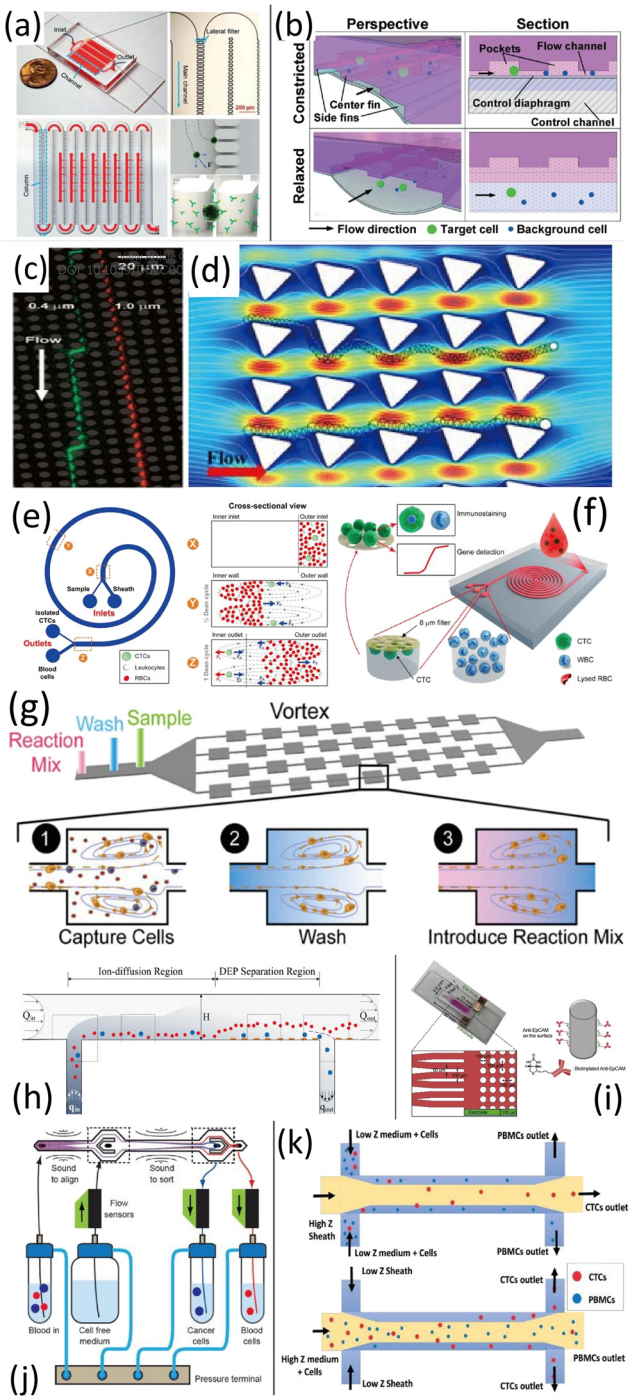

Fig. 5 Microfluidic methods for isolating CTCs: filtration methods ((a): a lateral filter array microfluidic device; adapted from ref. 82 with permission from John Wiley and Sons, copyright 2019. (b): Weir-based microstructures; adapted from ref. 83 with permission from Royal Society of Chemistry, copyright 2015), hydrodynamics methods ((c): micropillar deterministic lateral displacement array; adapted from ref. 84 with permission from The American Association for the Advancement of Science, copyright 2004. (d): Rotated triangular micropillars chip; adapted from ref. 85 with permission from John Wiley and Sons, copyright 2017. (e): Spiral microfluidic platform.[86] (f): Double spiral microchannel microfluidic platform; adapted from ref. 87 with permission from Springer Nature, copyright 2015. This panel also adapted from ref. 1 with permission from Royal Society of Chemistry, copyright 2020. (g): A vortex chip; adapted from ref. 88 with permission from *Proceedings of the National Academy of Sciences of the United States of America*, copyright 2018), dielectrophoresis methods ((h): dielectrophoretic field-flow-fractionation in a continuous-flow chamber; adapted from ref. 89 with permission from American Institute of Physics Publishing, copyright 2013. (i): ZonesChip; adapted from ref. 90 with permission from Elsevier, copyright 2019), and acoustic methods ((j): an automated microfluidic chip based on acoustophoresis; adapted from ref. 91 with permission from American Chemical Society, copyright 2017. (k): A label-free microfluidic chip based on acoustic impedance contrast; adapted from ref. 92 with permission from Royal Society of Chemistry, copyright 2018). This figure also adapted from ref. 1 with permission from Royal Society of Chemistry, copyright 2020.

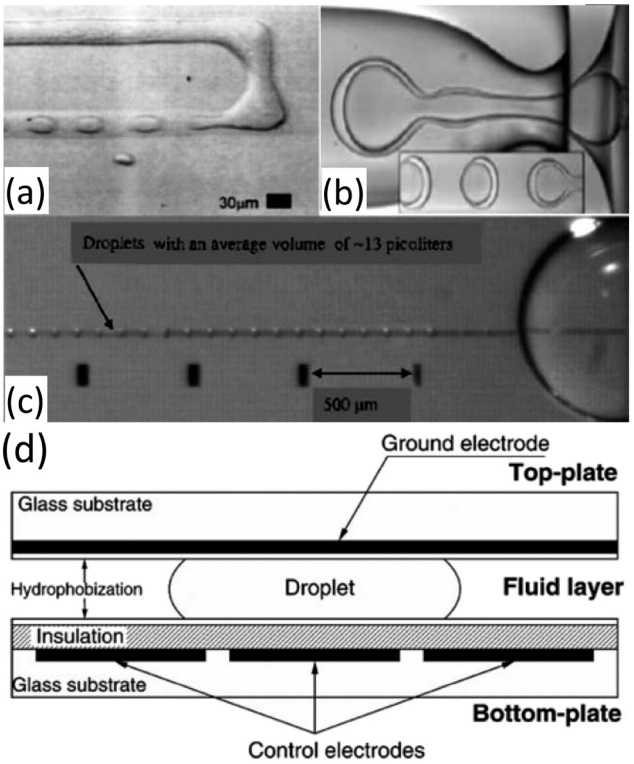

Fig. 6 Droplet formation mechanisms: (a) T-junction; adapted from ref. 108 with permission from American Physical Society, copyright 2001, (b) capillary focusing generation of oil/water/oil emulsion; adapted from ref. 109 with permission from The American Association for the Advancement of Science, copyright 2005, and (c) dielectrophoresis-based generation; adapted from ref. 110 with permission from Elsevier, copyright 2006. (d) This represents a schematic of a EWOD-based droplet device; adapted from ref. 111 with permission from Royal Society of Chemistry, copyright 2002. This figure also adapted from ref. 112 with permission from Royal Society of Chemistry, copyright 2008.

including dielectrophoresis and electrowetting on dielectric, enable highly precise droplet manipulation, the latter providing fine size control and widespread use in lab-on-chip systems[110,112,125] (Fig. 6).

Droplets can be efficiently mixed to accelerate reaction kinetics. *Passive mixing* relies on geometrically complex channels (*e.g.*, sharp turns, serpentine paths, and internal protrusions) that disrupt symmetry and induce chaotic advection with enhanced inter-droplet circulation[126–128] (Fig. 8). In contrast, active mixing applies external electrical signals, using electrowetting on dielectric devices (EWOD) method to oscillate, fuse, and split droplets, achieving complete mixing within seconds.[129]

Furthermore, sorting of droplets, which is crucial for purification and screening, is achieved *via* both passive and active mechanisms. Passive methods exploit gravity or channel geometry to separate droplets based on size[130,131] (Fig. 9). On the other hand, active sorting, such as dielectrophoresis or electrowetting on dielectric methods, manipulates electric fields to deflect or guide droplets with high precision.[132,133]

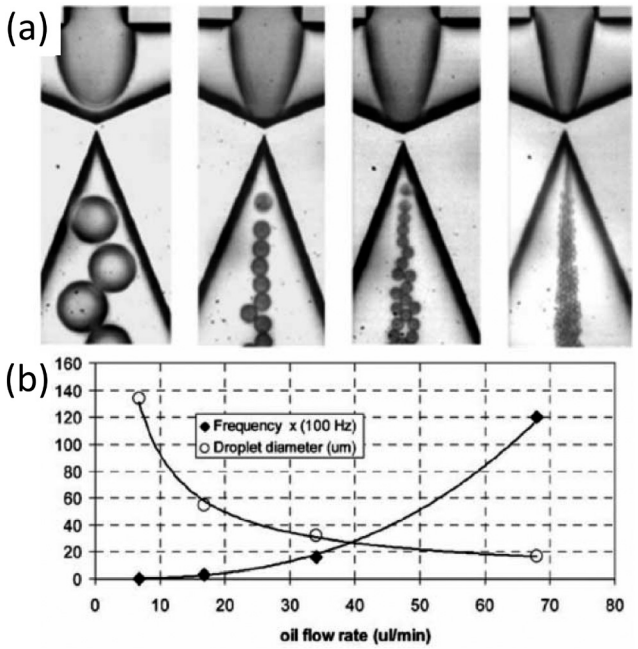

Fig. 7 (a) Generation of water-in-silicone oil droplets using an embedded circular orifice based on a flow focusing design. (b) The graph shows a decline in droplet size and a rise in formation frequency with an increase in oil flow rate. Adapted from ref. 113 with permission from Royal Society of Chemistry, copyright 2006.

4 Yield stress rheology in microfluidic technology

In many microfluidic applications, the working fluids exhibit yield-stress rheology. More broadly, couplings between microfluidics and complex fluids reveal new phenomena. Nghe *et al.*[136] demonstrated polymer breakup, near-wall flows, shear banding, and concentrated microgel suspensions in microchannels, where yield-stress effects (such as plug formation) were observed. Other studies have examined electrokinetic flows of yield-stress fluids,[137,138] drop formation with Carbopol,[139] and manipulation of biological fluids.[140]

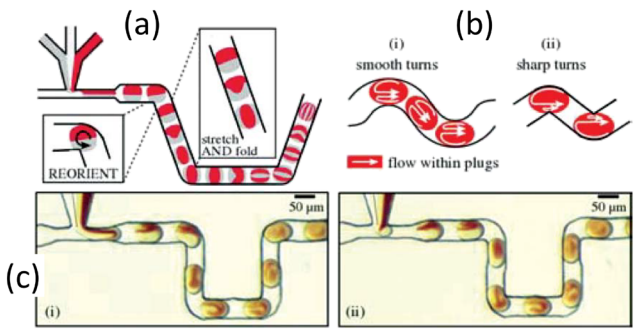

Fig. 8 Passive mixing within droplets. (a and b) Schematic demonstrating mixing patterns within droplets inside winding channels. (c) Experimental results show the rotational pattern. Adapted from ref. 114 with permission from Royal Society, copyright 2004.

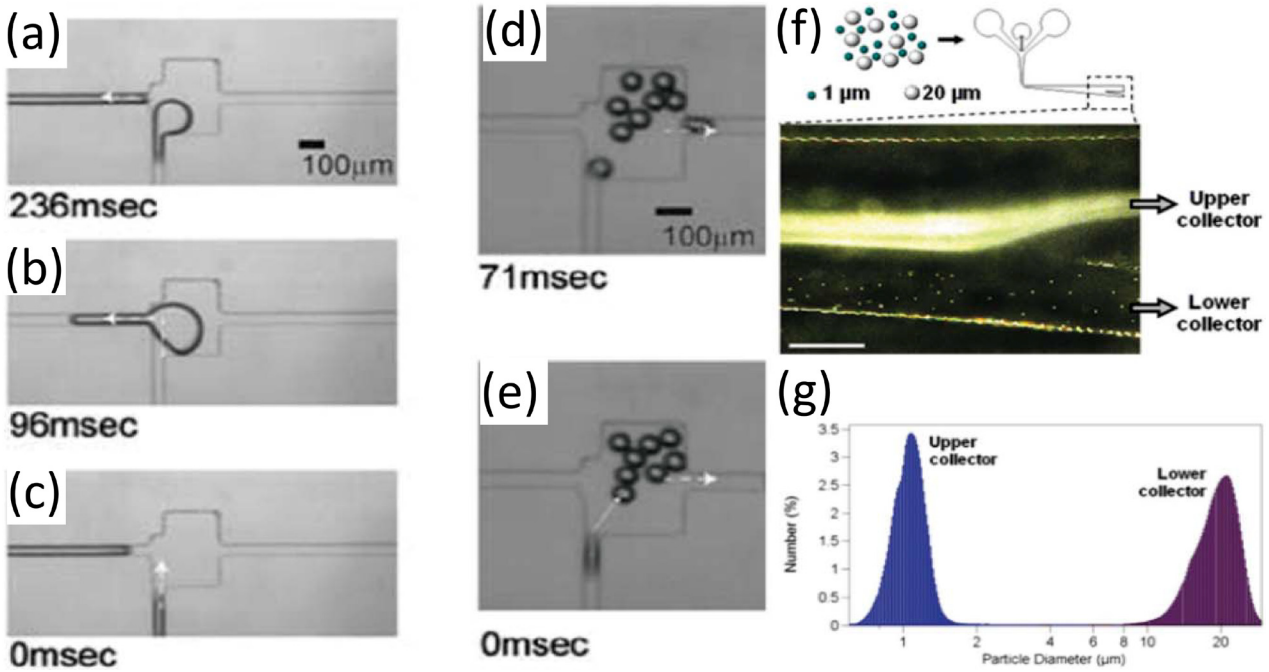

Fig. 9 Use of channel geometry for passive size-based sorting. Larger droplets transfer to the left channel (a–c) (white arrowhead). Smaller droplets transfer to the right channel (d and e) (white arrowhead). Size-based sorting based on sedimentation-effect; panels a–e are adapted from ref. 134 with permission from Springer Nature, copyright 2007. (f) Top-schematic of loaded particles into the system. Bottom-micrograph of expanding area of separation illustrates distinct separation. (g) Collected particles show high efficiency in sorting; panels f and g are adapted from ref. 135 with permission from American Chemical Society, copyright 2007. This figure also adapted from ref. 112 with permission from Royal Society of Chemistry, copyright 2008.

Microfluidics has also been applied to rheological measurements, advancing the concept of "rheology on a chip".[136,141] Additional devices have been also developed for passive mixing[142–144] and for particle fractionation and manipulation.[145–147] This section highlights the necessity of rheological considerations in microfluidic applications of complex fluids.

4.1 Role of yield stress rheology in CTCs separation

As noted, blood exhibits yield-stress behaviour alongside other complex properties such as viscoelasticity. Also, we highlighted the separation of CTCs from patient blood in section 3.1. While many microfluidic applications involve synthesising blood analogues or separating cells and particles from complex suspensions, we focus on CTC separation owing to its clinical importance, and here consider how the yield-stress behaviour of blood may affect separation quality.

In filtration-based methods of CTC separation, blood is passed through membrane filters or microstructured media, where CTCs are retained due to their larger size relative to other blood cells. A major challenge in such systems is clogging, which can be exacerbated by the yield-stress behaviour of blood. As discussed, this arises primarily from red blood cell aggregation and rouleaux formation, promoted at low shear rates and facilitated by plasma fibrinogen, a key clotting protein that bridges cells.[148–150] Accordingly, filter design must consider not only cell size but also the distribution of low-shear regions, where rouleaux can generate local yield-stress behaviour. These regions may evolve into unyielded zones of stagnant blood adjacent to microstructures, effectively altering the intended geometry and performance of the filter. Low-shear pockets between microstructures can likewise promote rouleaux formation[25,151] and moving plug zones, further worsening clogging and reducing device efficiency. Thus, blood yield-stress properties directly influence filtration performance in CTC separation.

Similar effects arise in hydrodynamic-based CTC separation, where CTCs are directed into distinct flow streams from other cells due to inertial force balance. In deterministic lateral displacement, blood passes through arrayed obstacles: smaller cells navigate the gaps, whereas larger CTCs are displaced into separate streams. However, rouleaux formation upstream can impair separation efficiency, making it essential to avoid low-shear regions there. Along streamlines, rouleaux formed under low shear (see the low shear-rate effects shown in Fig. 2) may also obstruct flow and compromise performance. Beyond yield-stress effects, blood viscoelasticity further influences separation. This viscoelasticity arises from both the elastic rouleaux network (and red blood cells themselves) and the viscoelastic nature of plasma.[152,153] Plasma elasticity in particular can trigger well-known instabilities even at very low velocities,[154,155] generating secondary vortices that perturb streamlines and reduce the quality of CTC

separation. In the other words, elastic instabilities can trigger chaotic flow streamlines, which must be considered when designing CTC separation devices that rely on laminar, predictable flow.

Dean flow fractionation exploits secondary flows in spiral microchannels, where centrifugal forces generate counter-rotating vortices across the cross-section. These vortices drive CTCs toward the inner wall while smaller blood cells migrate outward. In such flows, fluid rheology is crucial. Viscoelasticity is known to alter Dean flow structure, promoting the formation of additional smaller vortices[156,157] (see Fig. 10a), and, thus, the viscoelastic nature of blood can strongly affect CTC separation. At the same time, local shear rates may drop where these vortices form, favouring rouleaux aggregation and yield-stress effects. This can produce unyielded regions near the outer wall, analogous to stagnant plugs observed for yield-stress fluids in curved pipes and ducts.[158]

Micro-vortexing is a hydrodynamic separation method in which blood passes through sudden expansion–contraction zones, exposing CTCs to strong shear-gradient lift forces. This generates two vortices away from the main stream that trap the larger CTCs, which enables their separation. However, low shear regions at the expansion–contraction corners can promote rouleaux aggregation and yield-stress effects, forming unyielded zones (see the flow of a yield-stress fluid in a expansion–contraction chamber in Fig. 10b). The viscoelastic nature of plasma further favours such regions and can introduce instabilities, complicating the topology of unyielded plugs. Together, yield-stress and viscoelastic effects may hinder vortex trapping and reduce device efficiency.

Dielectrophoresis (DEP) exploits dielectric differences between CTCs and other blood cells. A non-uniform electric field is applied so that the larger CTCs experience DEP forces exceeding fluid drag, enabling their isolation. However, blood viscoelasticity can induce instabilities and additional forces on CTCs, affecting downstream separation. Rouleaux formation further complicates isolation, since aggregates may exhibit dielectric properties distinct from individual cells. In acoustic methods, ultrasonic resonances generate forces that depend on cell size, density, and deformability, directing CTCs along different trajectories from other blood cells. Here too, rouleaux formation and plasma viscoelasticity alter the force balance on CTCs, reducing separation quality.

Finally, we should mention that for all the above methods, the influence of low shear rate regions that may lead to rouleaux formation strongly depends on the characteristic length of such regions compared to the size of the red blood cells. In fact, the rouleaux formation and, thus, appearance of unyielded plug region are more probable when the characteristic length of the region with low shear rate is sufficiently larger than the size of red blood cell.

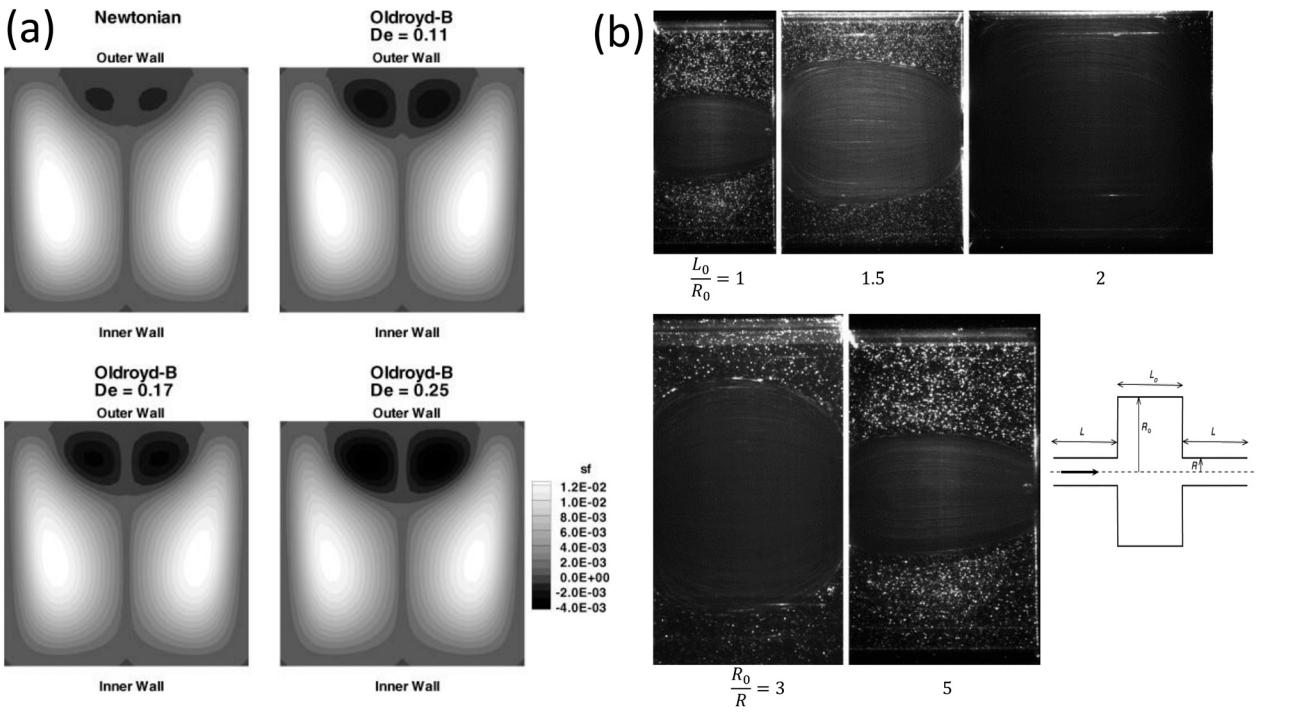

Fig. 10 (a) Effect of fluid viscoelasticity on Dean vortices at three Deborah numbers (De = 0.11, 0.17, and 0.25), with the Dean number fixed (Dn = 150). Results are compared with the Newtonian-fluid counterpart. Adapted from ref. 157 with permission from Elsevier, copyright 2009. (b) Effect of geometry on the flow of a yield-stress fluid (Carbopol gel) in an expansion–contraction chamber. In each case, the flow is from left to right, and the illuminated regions at the bottom and top indicate unyielded (stagnant) zones, whereas the flow is yielded in the central region. Adapted from ref. 159 with permission from Elsevier, copyright 2007.

4.2 Yield stress fluid in bioprinting

As noted in section 3.2, droplet microfluidic systems generate, merge, mix, and split fluid droplets by injecting one phase into another immiscible carrier. Droplet size is strongly influenced by the viscosity ratio between the phases and by surface tension variations arising from surfactants; thus, the rheology of both dispersed and continuous phases critically affects droplet formation. Both phases may exhibit yield-stress behaviour, making rheological characterization before and after surfactant addition essential. In bioprinting, similar considerations apply: in both direct ink and embedded printing, the rheology of the ink and the supporting bath governs print fidelity, as highlighted in several reviews.[160–162] This section further examines the role of rheology in bioprinting applications.

Numerous reviews have emphasized the importance of ink rheology in direct ink writing (DIW).[160,161,163] Key parameters are shear-thinning, yield stress, and viscoelasticity, all of which govern print quality (Fig. 11) (thixotropy can be also relevant). For example, shear-thinning, which arises from chain disentanglement/extension and weakened intermolecular interactions, ensures smooth nozzle flow under shear and rapid viscosity recovery post-deposition, allowing filaments to retain shape and fine features.[160] Also, yield stress is equally critical: the static yield stress defines the minimum threshold for extrusion, whereas the dynamic yield stress sustains filaments against gravity and capillarity.[160] Inks must exceed the static value to flow, yet maintain sufficient dynamic yield stress to resist sagging, oozing, and deformation, thereby supporting subsequent layers. A balanced flowability is thus required. Viscoelasticity also plays a central role. A wide linear viscoelastic range is desirable, as it allows storage and loss moduli (G', G'') to remain constant over larger strains, reducing nonlinear softening, yielding, and creep during processing.[164,165] This reflects a robust network resistant to bond slippage, broadens the processing safe zone, and improves filament stability. Minimal thixotropy is also preferred, ensuring rapid viscosity response to shear-rate changes for smoother extrusion and deposition.[161]

Ink properties have been enhanced through additives such as cellulose nanofibrils (CNFs). For example, CNFs incorporated into *Aloe vera* gels increased G' and G'' while

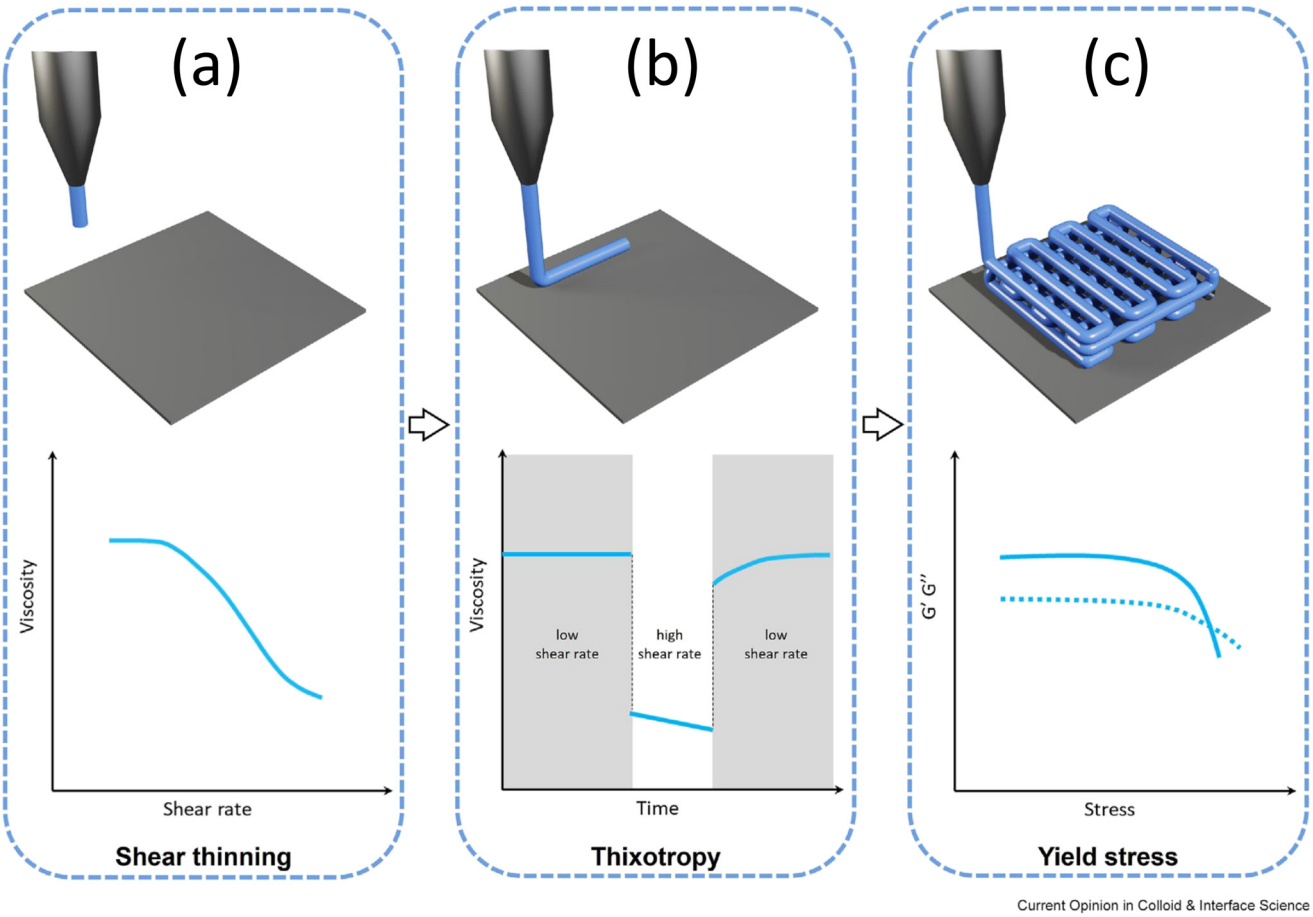

Fig. 11 Schematic description of direct ink printing, highlighting the important role of ink rheology in different stages of printing. (a) Favorable shear-thinning effect on the ink flow-ability at the early stage of printing. (b) Significance of ink thixotropy (less thixotropic is more favorable) at the printing stage when the ink settles on the substrate. (c) Yield stress and viscoelasticity effects on the quality of the printed structure. Adapted from ref. 161.

imparting shear-thinning and optimal yield stress.[164] Erfanian *et al.*[167] produced a conductive ink by combining CNFs with graphene nanoparticles, achieving viscosity reductions by five orders of magnitude and ensuring smooth nozzle flow; here, G' exceeded G'' by an order of magnitude, improving post-printing stability. Similarly, chitosan/graphene oxide hydrogels exhibited enhanced viscoelasticity due to nanosheet–polymer interactions, with increased graphene oxide concentrations further boosting viscosity and yield stress.[168] In extrusion bioprinting, CNFs contribute not only to printability but also to the biological and structural function of constructs by providing a fibrillar, ECM (extracellular matrix)-mimetic microenvironment that can guide cell organization and by improving post-deposition shape fidelity *via* rapid stabilization in composite systems (*e.g.*, CNF–alginate).[169]

Models have recently been developed to study the spreading of a single droplet and a filament of a yield-stress fluid on a solid surface.[170,171] Jalaal *et al.*[171] developed scaling laws, complemented by an asymptotic analysis for shallow droplets, to predict the final equilibrium shape of a spreading yield-stress droplet under the combined effects of surface tension and gravity. van der Kolk *et al.*[170] showed that the final filament shape is governed by a competition between surface tension (the driving force) and yield stress (the resisting force), and they presented a scaling law for the final filament width. Together, these studies highlight the critical role of yield stress in determining the final shape of printed droplets and filaments, suggesting that yield stress is an important design parameter.

Embedded bioprinting into a yield-stress bath, to enable precise patterning of soft, low-viscosity inks with high fidelity, has gained increasing attention.[162,166,172–174] Their applications span from food production to soft robotics.[162]

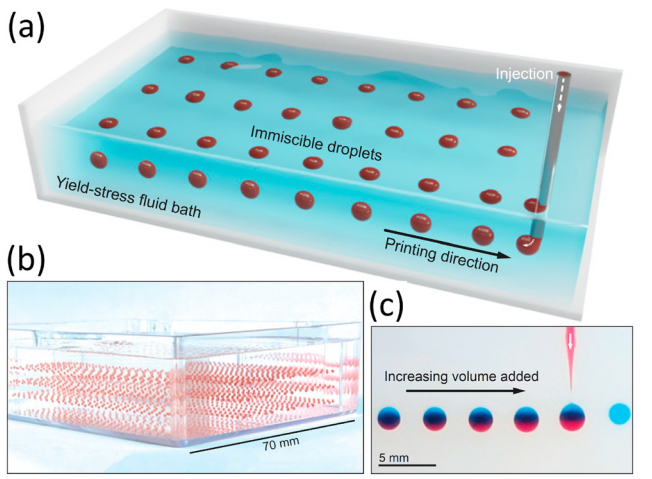

Fig. 12 Schematic description of embedded droplet printing. (a and b) Suspended red-dyed droplets are formed in a bath of yield-stress fluid. (c) A red aqueous solution is injected into previously printed blue aqueous droplets. Adapted from ref. 166 with permission from *Proceedings of the National Academy of Sciences of the United States of America*, copyright 2020.

Nelson *et al.*[166] introduced embedded droplet printing, generating droplets that remain undisturbed by external flow or rigid boundaries by exploiting yield-stress rheology (Fig. 12). This capability, *i.e.*, significant for processes such as pharmaceutical crystallization, permits printing and long-term manipulation of suspended droplets in bulk pools, unconstrained by geometry. Embedding in yield-stress baths also prevents droplet motion or coalescence without surfactants, avoiding convective and boundary effects common in other systems. Brunel *et al.*[172] further showed that ink microstructure can be tuned through ink–bath interactions. Incorporating structural features of the support bath into the printed ink produced porous voids after bath removal, with porosity governed by the viscosity ratio between ink and support. Finally, as an emerging voxel-based approach, all-aqueous printing of viscoelastic droplets in yield-stress media, allows digital placement of spherical bio-ink particles to construct functional tissue analogues.[175] Zhu *et al.* demonstrated that print fidelity depends on both nozzle acceleration and droplet/nozzle diameter ratio, with high fidelity achieved for large droplet/nozzle ratios and intermediate accelerations.

This section highlighted the critical role of ink rheology in bioprinting, encompassing both direct-ink writing and embedded printing. As discussed, precise control of ink rheology (*i.e.*, yield stress, shear-thinning, viscoelasticity, and thixotropy) is required at different stages of printing, underscoring the need to study the complex fluid mechanics of bioprinting.

4.3 Yield stress rheology and electrorheological fluids

Electrorheological (ER) fluids, *i.e.*, produced by suspending dielectric particles in insulating oils, are smart colloids whose viscosity can be tuned by external electric fields.[176] Under field application, particles organize into columnar structures, imparting yield-stress behaviour.[176] ER fluids have enabled chip-embedded soft valves, and this is advancing fluidic-based automatic droplet control.[176] Typical dielectric particles include TiO_2, calcium, strontium, and carbon nanotube hybrid polymers.[176] Yield stresses up to 300 kPa can be achieved, *i.e.*, sufficient for digitally controlling microvalves.[176] Fig. 13 illustrates ER fluid behaviour before and after field application: without a field the suspension flows, while with a field particle columns form, generating yield stress. This figure also shows practical implementations of giant ER fluids for droplet generation.

ER fluids are particularly well-suited to microfluidic platforms because they enable on-demand, spatially localized tuning of viscosity and apparent yield stress under modest voltages applied across micron-scale electrode gaps, facilitating compact implementations of valves, pumps, and flow resistors without moving parts. In addition, the strong field gradients achievable in microchannels allow ER fluids to be used for selective particle/cell manipulation and reconfigurable flow routing (*e.g.*, field-driven focusing,

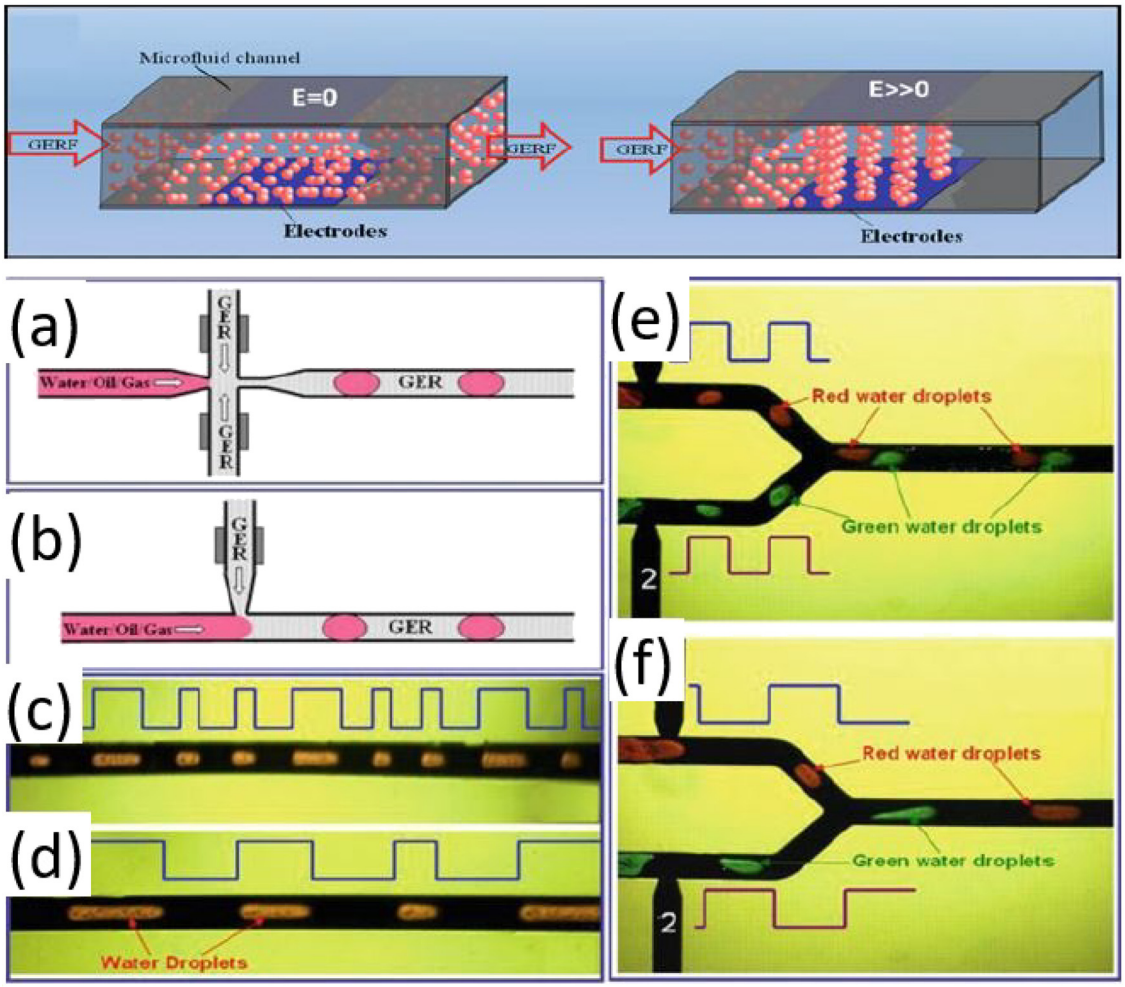

Fig. 13 Giant ER fluid flow before and after applying the electric field. (a–d) Giant ER fluid-assisted droplet generation: (a) flow-focusing approach; (b) T-junction. (c and d) Electric-field-controlled generation of droplets. (e and f) Digitalized controlled droplets distance. Adapted from ref. 176 with permission from Springer Nature, copyright 2011.

trapping, and switching), making ER fluids a practical route to active control in lab-on-a-chip systems.

There are many reviews on ER fluids.[177–181] Sheng and Wen[181] comprehensively reviewed ER fluids, distinguishing classical dielectric ER (DER) systems, governed by induced dipoles, from giant ER (GER) systems, *i.e.*, dominated by orientational polarization of molecular dipoles. They also outlined a continuum ER hydrodynamics framework and emphasized how strong, millisecond-scale ER responses enable on-chip digital control elements such as droplet logic, pumps, and valves. Their work set the stage for constitutive modelling (*e.g.*, field-dependent yield stress) and device-level microfluidics exploiting tunable yield-like behaviour. In addition, Hong and Wen[180] provided an application-oriented perspective, showing how carrier-oil chemistry (*e.g.*, hydrogenated silicone oils) and particle–liquid affinity govern chain development and amplify GER responses. By contrasting wetting and non-wetting suspensions and linking these to device integration (*e.g.*, microvalves, mixers, and other components), they established practical design rules for embedding ER working fluids into microfluidic platforms. More recently, Munteanu *et al.*[177] reviewed key aspects of ER fluids, surveyed commonly used ER materials and liquid carriers, and summarized representative dielectric particles and composites. They tabulated particle characteristics and ER performance, and outlined the main requirements, advantages, and limitations of state-of-the-art ER fluids. An another recent work, Park and Choi[178] comprehensively reviewed sensors and sensing devices that used ER fluids and magnetorheological (MR) materials, whose stiffness and damping were tunable *via* external stimuli.

On the constitutive modelling side, Hao[182] re-examined the origin of ER yield stress and proposed an expression where both polarization and conduction losses contribute to field-induced resistance to flow. This model rationalises material-to-material variability, including anomalies such as $BaTiO_3$ in silicone oils, and links the observed Bingham-like response to dielectric and conductive contrasts between particles and carrier liquid. The yield criterion was derived

from energy dissipation arguments and compared with earlier conduction model bounds. More recently, Chung *et al.*[183] developed a unified scaling for ER yield stress by recasting the interplay of field strength and microstructure into a dimensionless form. Their composite law transitions smoothly from low- to high-field regimes, collapsing data across chemistries and particle sizes. Conceptually, this bridges dipolar chaining and conduction-enhanced interactions, yielding a single curve for $\tau_y(E)$ directly applicable to device-level design.

Turning to viscoelasticity, Dhar *et al.*[184] studied agarose-based organic ER suspensions, to prob time-dependent mechanics under field through steady, creep, stress-relaxation, and oscillatory tests. Increasing E elevated the apparent yield stress (approaching ~kPa) and induced a fluid-to-solid transition with electro-thixotropic hysteresis. Fractional-derivative fits captured the field-tunable elastoviscous spectra, attributing memory and dissipation to field-controlled assembly and disassembly of chain networks. Ishii *et al.*[185] examined polyurethane-based, ion-conductive ER systems to link polymer physics with electrorheology. By tuning glass transition and ionic pathways within polymer inclusions, they showed how electrolyte content and segmental mobility govern both yield stress and linear viscoelastic response under E. Their approach combined materials design (ionically conductive elastomers) with small-amplitude rheology, demonstrating that higher ionic conductivity strengthens field-coupled structures, whereas polymer stiffening suppresses ER buildup.

Chaudhary *et al.*[186] isolated pure extensional rheology in a contraction–expansion microdevice by exploiting controlled wall slip to decouple shear and stretch. They identified two extensional regimes under field (*i.e.*, a low-rate viscous branch and a high-rate field-stiffened branch) with self-similar stress scaling at the transition. Imaging and pressure/flow data revealed slip-layer thinning as E increased, consistent with longer chains transmitting tensile loads along streamlines. Because interparticle interactions in ER fluids can be tuned externally by adjusting the electric-field strength, this work provides deeper insight into how interaction-induced jamming influences slip characteristics without changing particle concentration. This work opens new frontiers for a broad range of soft-jammed materials (including soft glassy materials) in which the degree of jamming can be tuned by controlling interparticle interactions, for example in thermo-responsive soft systems, polymer-grafted nanoparticles, and pH-responsive soft materials. This study also suggests that microdevice design is strongly correlated with the characteristics and dynamics of the ER fluid system.

At the device level, Qian *et al.*[187] engineered stepwise electrode fields in microchannels to program the nucleation, elongation, and jamming of chains. Combining high-speed visualization with pressure–flow measurements, they modelled field-driven microstructure growth and pressure drop, capturing both transient buildup and steady resistance. This demonstrates spatial programming of rheology within chips by tailoring electrode geometry and field gradients.

Bhattacharya and Chakraborty[188] linked ER rheology with ion transport, showing that in variable-area microchannels, field-dependent viscosity can amplify and steer ion concentration polarization (ICP). A 1D area-averaged theory, validated by 3D simulations, revealed that stronger ER contrasts between channel sections, higher solute concentration, and larger axial fields magnify enrichment and depletion zones, identifying ER-enabled selectivity knobs for electrokinetic preconcentration and separation.

This section highlighted applications of ER fluids in microfluidic technology and discusses how rheological manipulation can be leveraged to achieve design goals. We also reviewed both recent and classic efforts to develop constitutive models of ER-fluid rheology.

4.4 Locomotion in complex fluids

Research on swimming and crawling in complex media now forms a coherent framework across theory, experiment, and bio-inspired design. Lauga[189] provided a concise theoretical perspective based on integral constraints for self-propulsion in non-Newtonian media, also clarifying what complex rheology can and cannot offer at small scales. Godon *et al.*[190] reviewed locomotion on or through yielding terrains (*e.g.*, muds, slurries), organizing animal and robotic strategies by body–substrate interaction and identifying engineering opportunities. More recently, Hewitt[191] synthesized locomotion in yield-stress fluids, and highlighted slender-body theory, data comparisons, and the central role of localized plastic deformation in determining speed and efficiency.

A central theoretical theme is how yield stress alters classical Stokes-regime propulsion. Extending Taylor's waving sheet, Hewitt and Balmforth[191,194] showed that finite yield stress confines deformation to a layer on the wavelength scale, modifying the speed–stroke relation relative to Newtonian fluids. In asymptotic limits, plastic rheology can even yield higher normalized speeds for the same waveform. Generalizing to filaments, viscoplastic slender-body theory and its cylindrical, wavy extension mapped the interplay among wave amplitude, wavelength, and Bingham number. At small stroke, yield-stress dominance produces "plastic locomotion" with strong gait dependence, including regimes of reduced or reversed progress, whereas at large stroke swimmers can slide or burrow nearly along their centerline with relatively high efficiency.[195] Beyond slender bodies, squirmer models solved in yield-stress media[191,193] complement slender-body predictions, showing how surface slip-mode composition and yield stress jointly regulate propulsion and energetic performance (Fig. 15).

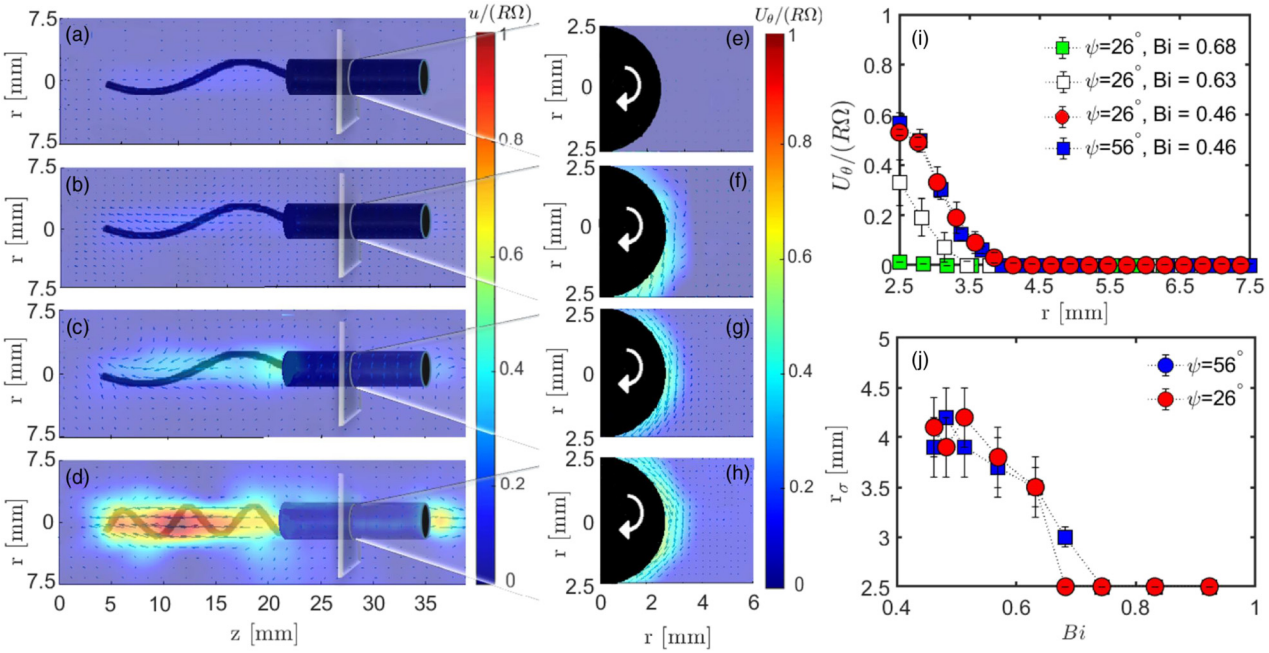

Fig. 14 Locomotion of a helical squirmer in a yield stress fluid. Time-average 2D velocity profiles (a–d) with corresponding profiles in normal to locomotion direction (e–h). ψ is the tail pitch angle, while Bi is the Bingham number. In this figure, (a and e) ψ = 26°, Bi = 0.68, (b and f) ψ = 26°, Bi = 0.63, (c and g) ψ = 26°, Bi = 0.46, and (d and h) ψ = 56°, Bi = 0.46. (i) Angular velocity profile *versus* the radial location around squirmer's head; (j) yield surface location (r_σ) as a function of Bingham number. Adapted from ref. 192 with permission from American Physical Society, copyright 2023.

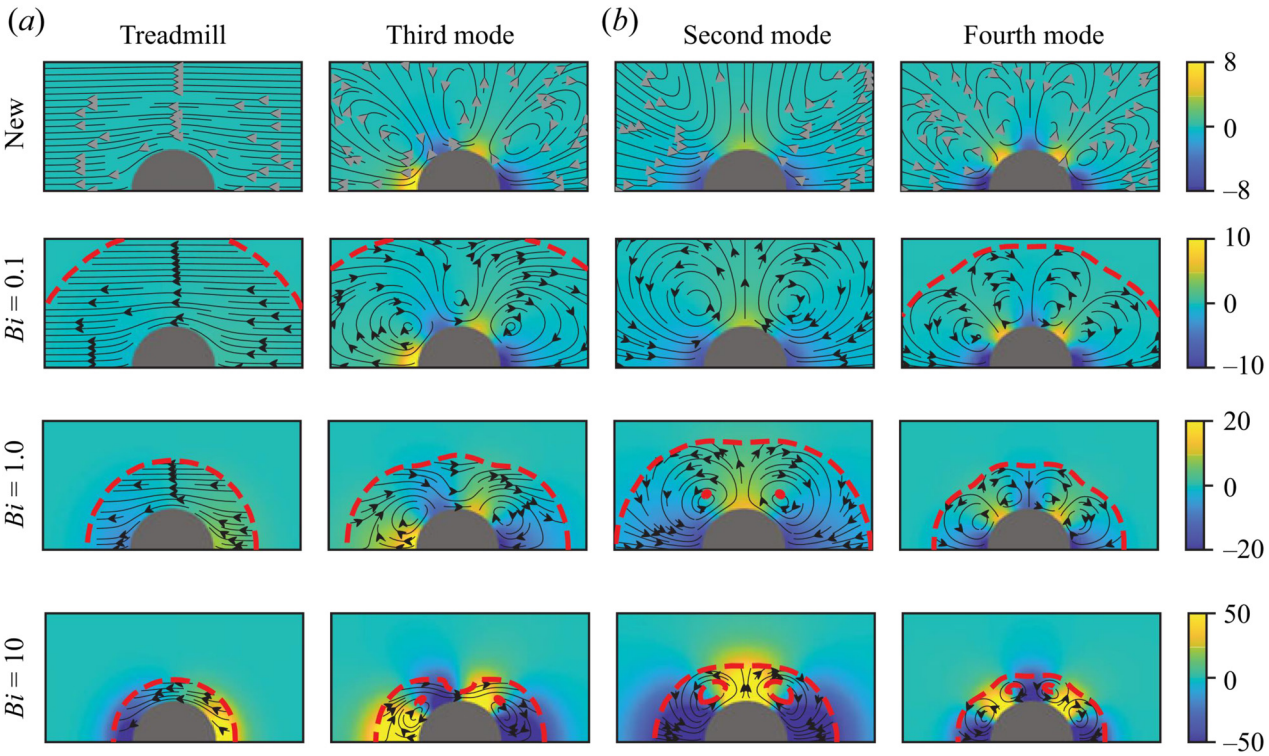

Fig. 15 Flow field around an squirmer in a yield stress fluid; shown for (a) even and (b) odd stroke modes. The yield surface is shown by red dashed line. Adapted from ref. 193 with permission from Cambridge University Press, copyright 2022.

Experiments have tested these theoretical predictions. Using magnetically driven fixed-geometry helices in Carbopol gels, Nazari *et al.*[192] identified two thresholds: a minimum torque to initiate rotation (*i.e.*, marking the local transition

from elastic network to yielded region) and a higher criterion for sustained translation. Measurements showed a compact yielded envelope around the helix, bounded by unyielded material, and speed-gait maps revealing optimal pitch angles and rotation rates specific to yield-stress environments (Fig. 14). These results accord with theory: thresholds reflect yielding onset, while the confined sheared layer explains pronounced axial motion at comparatively modest energetic cost.[191]

Crawling on thin complex-fluid films provides a complementary mode of locomotion, central to adhesive crawling and relevant to wall-bound microrobots. Chan *et al.*[196] combined lubrication models with benchtop crawlers to identify two mechanisms: pressure-driven motion on Newtonian films and yield-stress-mediated motion (LAPONITE®) enabling vertical and inverted crawling. In the latter, wave zones exceed the yield stress and slide, while interwave regions remain solid-like and anchor the crawler. They demonstrated that devices can climb and traverse ceilings when film rheology (yield stress and restructuring) is tuned appropriately. Complementary studies on pedal mucus and bio-inspired simulants established design criteria: reliable climbing requires high yield stress for support, low post-yield viscosity for speed, and short restructuring times for rapid re-adhesion.[197]

Locomotion in viscoelastic liquids (without yield stress) highlights fluid memory. Combining high-speed imaging of *Chlamydomonas* with simulations using the measured stroke, Li *et al.*[198] showed that elastic stresses feed back on gait and stress distribution, modifying performance relative to Newtonian flows. Their framework links speed changes to the structure and strength of elastic stresses generated by the real waveform. This complements the viscoplastic picture: elasticity reshapes stresses over a cycle, whereas yield stress imposes spatial and temporal thresholds that compartmentalize the flow.

These insights suggest several microfluidic strategies. Yield thresholds can serve as functional gates or *in situ* material probes: swimmer-onset criteria provide direct readouts of local yield strain or stress, enabling embedded microrheometry in gels and biofluids.[192] Helical microrobots offer geometry-tunable "cutting" through viscoplastic matrices for targeted delivery or biopsy in mucus-like media, with pitch and frequency tuned near measured optima.[192,195] For surface-bound transport and pumping, adhesive-style crawling motivates thin-film designs balancing yield stress (support/adhesion) against post-yield viscosity, while exploiting rapid restructuring to reset contact, criteria already quantified in mucus and Carbopol/LAPONITE® gels.[196,197] In viscoelastic channels, coupling measured gaits to elastic stress predictions enables waveform-aware micromixers and cell-compatible pumps that harness fluid memory.[198] Thus, complex-fluid rheology is not a nuisance but a design parameter: by aligning stroke, geometry, and medium, one can shift from being trapped by unyielded plugs to exploiting localized flows for efficient, targeted motion.

4.5 Slip of complex fluid in microscale

Lauga *et al.*[199] established the Newtonian baseline by reframing no-slip as an assumption rather than a law and cataloguing interfacial conditions under which it fails at small scales. They showed how wettability, roughness, pressure, charge, dissolved gas, and contamination can all induce apparent slip, and consolidated measurement approaches (*i.e.*, from pressure–flow assessments to local velocimetry and molecular simulations) within the Maxwell–Navier slip-length framework. This provides the methodological and conceptual reference for isolating non-Newtonian effects. Malkin and Patlazhan[200] addressed complex fluids, arguing that rheology itself governs wall slip in microscale flows. They identified two bulk pathways coupling to boundaries: (i) viscoplastic solid-to-fluid transitions near yielding that enable interfacial sliding, and (ii) flow-induced structural changes (*e.g.*, disentanglement or lubrication-layer formation; see Fig. 16) that generate near-wall depletion and apparent slip. Their synthesis unified results across polymeric liquids, colloidal gels, and concentrated suspensions, showing that identical surface treatments can yield different slip responses depending on the constitutive behaviour.[200]

For polymer melts, Hatzikiriakos[201] showed that slip begins above a critical wall shear stress and can shift from weak to strong regimes as chains detach and interfacial entanglements fail. Slip velocity depends on molecular weight, temperature, normal stresses, and surface chemistry, motivating stress-dependent, material-specific boundary conditions rather than a universal Navier slip length. This polymer-centric physics illustrates how viscoelasticity alters slip length and onset relative to Newtonian predictions.

From a broader soft-matter perspective, Bonn *et al.*[9] emphasized that in yield-stress materials, wall slip, shear heterogeneity, and nonlocal effects are inseparable under confinement. Measured flow curves thus require attention to yielding, aging, and boundary-condition sensitivity. In microfluidics, where confinement is strong, these couplings are amplified and slip may dominate observed kinematics unless explicitly quantified and controlled. Nghe *et al.*[136] highlighted that low-Reynolds but high-Weissenberg-number flows are common on chips, making elastic effects and flow–structure coupling accessible without turbulence. Their review spans polymer-solution flows near walls, shear

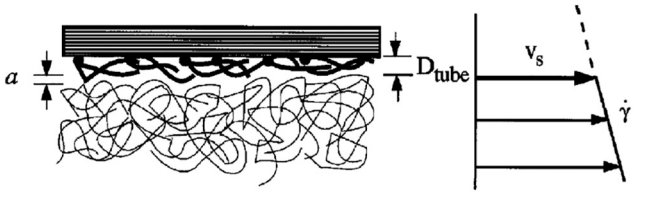

Fig. 16 An illustration of a layer of stretched molecules near the wall, which is responsible for the core layer slippage with slip velocity V_s. Adapted from ref. 200 with permission from Elsevier, copyright 2018.

banding in microchannels, and microgel transport, showing how wall slip, depletion layers, and confinement encode constitutive behaviour at micrometre scales.

Translating this framework into targeted experiments, Younes *et al.*[202] quantified slip of a model yield-stress microgel (Carbopol) in straight microchannels using epifluorescence velocimetry. They derived scaling laws for wall velocity gradient and slip velocity across full-plug, partial-plug, and fully yielded regimes, and assessed wall-chemistry treatments to suppress slip. Their data linked slip to near-wall solvent depletion and connected interfacial kinematics to bulk yielding through wall-stress scaling. Confinement amplifies such couplings. Using PIV in quasi-square channels from ~450 to ~50 μm, Liu *et al.*[203] showed that large channels follow Herschel–Bulkley fits, whereas channels ≲150 μm exhibit velocity profiles inconsistent with a finite yield stress and are better captured by power-law (zero-yield) models. Confinement also inverted effective slip trends as microstructure adjusted, demonstrating that slip and apparent rheology co-evolve when channel dimensions approach structural length scales. In confined geometries, velocity profiles of jammed soft materials often cannot be captured by a strictly local constitutive relation, because plastic rearrangements couple over a finite spatial range. This motivates non-local descriptions introducing a cooperativity length (*e.g. via* a fluidity field) to represent wall-to-bulk coupling and spatially correlated yielding. Such confinement-driven non-locality was demonstrated experimentally in microchannels by Goyon *et al.*[204,205] and discussed in detail in the review of Mansard and Colin.[206] Beyond steady flows, extensions to transient regimes have been actively developed in recent years; see the review by Benzi *et al.*[207] These works provide the appropriate context for interpreting the observations reported by Liu *et al.*[203] in confined configurations. In several recent works, the non-local fluidity was reported for jammed soft materials.[208–210] The role of directional roughness, introduced *via* a herringbone pattern on a microchannel wall, was studied by Filippi *et al.*[208] From the 3D velocity profiles across the channel, the authors reported that the stress field emerged as strongly heterogeneous and banded, consistent with nonlocal correlations.[208] Guastella *et al.*[209] investigated how wedge-shaped microroughness activated emulsion droplet fluidization in pressure-driven microchannel flow. Using maskless photolithography to texture one wall, they measured velocity profiles for flow aligned with and against the wedge ramps. Flow along the climbing ramp was enhanced as the pressure gradient increased, yielding up to a 30% higher volumetric flow rate than in the opposite direction, depending on the pressure drop.

To decouple constitutive response from boundary effects, Gupta and Vanapalli[211] used 3D digital holographic particle tracking in linear microchannels to reconstruct flow without assuming no-slip. Their microfluidic shear rheometer produced viscosity–shear-rate curves for Newtonian and PEO solutions using ~20 μL samples over 5×10^{-2}–2×10^{4} s^{-1} and directly revealed finite slip lengths (~3–5 μm) in highly viscoelastic PEO. Their method demonstrates how optical velocimetry can measure through slip rather than be confounded by it, confirming that viscoelasticity promotes measurable interfacial slip even on nominally wetting walls. Dynamic protocols highlight similar principles. Medina-Bañuelos *et al.*[212] combined oscillatory rheometry with PIV (Rheo-PIV) on a viscoplastic microgel, identifying a critical stress for slip onset under both oscillatory and steady conditions. At low frequencies, slip produced phase shifts and Bowditch–Lissajous "mango" loops; importantly, plate-strain signals diverged from true, PIV-measured strain once slip set in, yielding a procedural map for diagnosing and deconvolving slip in oscillatory tests of yield-stress fluids. Finally, Kavishvar and Ramachandran[65] developed a Hele–Shaw microfluidic extensional device that estimates very low yield stresses (10 mPa–1 Pa) from the size of a central unyielded region. Validated on Carbopol, blood, and mucus simulants, this imaging-based scaling avoids wall-shear extrapolation and provides real-time, low-volume τ_y estimates precisely in slip-dominated regimes.

Overall, these studies deliver the message that, beyond Newtonian liquids, microscale slip is a rheology-conditioned phenomenon shaped by yielding, elasticity, structural depletion, and confinement-altered constitutive laws. Resolving near-wall kinematics (PIV/DHM), controlling wettability, and exploiting extensional microflows are essential for quantifying slip in complex fluids, where boundary conditions and bulk rheology must be treated as a coupled system.[9,136,199–201]

4.5.1 Complex fluid and superhydrophobicity-driven slip. Rahmani and Taghavi[213] reviewed how wall slip can be engineered *via* superhydrophobic (SH) surfaces and exploited in microfluidics to reduce viscous losses in pumping, mixing, or separation. Slip arises when wall texturing traps gas, creating a near shear-free liquid–gas interface that yields a finite slip length and drag reduction. While Newtonian slip over SH surfaces is well established, the review highlights a key gap: few studies address how complex (non-Newtonian, viscoelastic, or viscoplastic) fluids slip over SH textures, motivating further work.

Haase *et al.*[214] numerically studied shear-thinning Carreau fluids in channels with spanwise bubble mattresses, resolving curved liquid–air interfaces and quantifying slip length and flow rate *versus* texture fraction and speed. They found that (i) shear thinning amplifies apparent slip relative to Newtonian flow, and that (ii) slip enhancement can be non-monotonic in flow rate (Carreau number) due to concentrated shear and depleted viscosity near texture edges. Patlazhan and Vagner[215] extended this to Carreau–Yasuda fluids over longitudinal and transverse SH stripes, using simulations and a three-zone model (high-shear, low-shear, outer) to rationalize anisotropic responses. They showed larger slip for longitudinal textures and likewise predicted non-monotonic slip–shear dependence. Overall, shear thinning can markedly increase effective slip, but its

magnitude and anisotropy depend strongly on stripe orientation and gas fraction.

Ray *et al.*[216] analyzed weakly shear-thinning Carreau fluids over longitudinal SH grooves *via* asymptotic integral relations and simulated strong shear-thinning cases matched to blood and xanthan. They showed that SH-induced shear localization at groove edges drives viscosity reduction and slip, yielding a robust slip-length maximum at intermediate Carreau numbers ($O(1)$–3), while decreasing solid fraction amplifies both localization and slip. Schnitzer and Ray[217] developed an asymptotic theory for giant slip, showing that in thin channels with large intrinsic SH slip, effective slip for power-law/Carreau-like fluids scales sharply with texture and rheological exponents, *i.e.*, transitioning from logarithmic growth (Newtonian) to algebraic amplification under strong shear-thinning. Their homogenization framework across longitudinal/transverse textures provides scaling laws that rationalize observed non-monotonic optima and clarify when geometry *versus* rheology controls drag reduction.

Rahmani and Taghavi[218] developed the first semi-analytical and numerical models for plane Poiseuille flow of Bingham fluids in thick channels with SH grooved walls, using a Navier slip condition to quantify how Bingham number, slip number, and gas fraction govern unyielded plug formation and effective slip length. They also showed, *via* perturbation analysis and simulations, that inertia breaks flow symmetry. Extending to the thin-channel limit under creeping motion, Rahmani and Taghavi[219] derived correlations and identified regimes where confinement deforms and breaks the unyielded center plug while increasing slip length (Fig. 17). Rahmani *et al.*[220] then examined inertial Bingham flow past transverse SH grooves, showing that higher Reynolds number diminishes dimensionless slip velocity but non-monotonically promotes plug breakage. Incorporating groove orientation, Rahmani and Taghavi[221,222] analyzed longitudinal, transverse, and oblique patterns, introducing metrics such as a mixing index and a slip-angle offset between pressure-gradient and slip-velocity directions. They found that increasing Bingham number shifts the optimum orientation angles for peak shear slip and mixing index to progressively smaller values, underscoring yield stress as a key design lever for steering and mixing in viscoplastic microflows. This unifying framework links longitudinal and transverse limits and clarifies why oblique SH (or chemically patterned) surfaces enable orientation-tunable slip and transport control at the microscale.

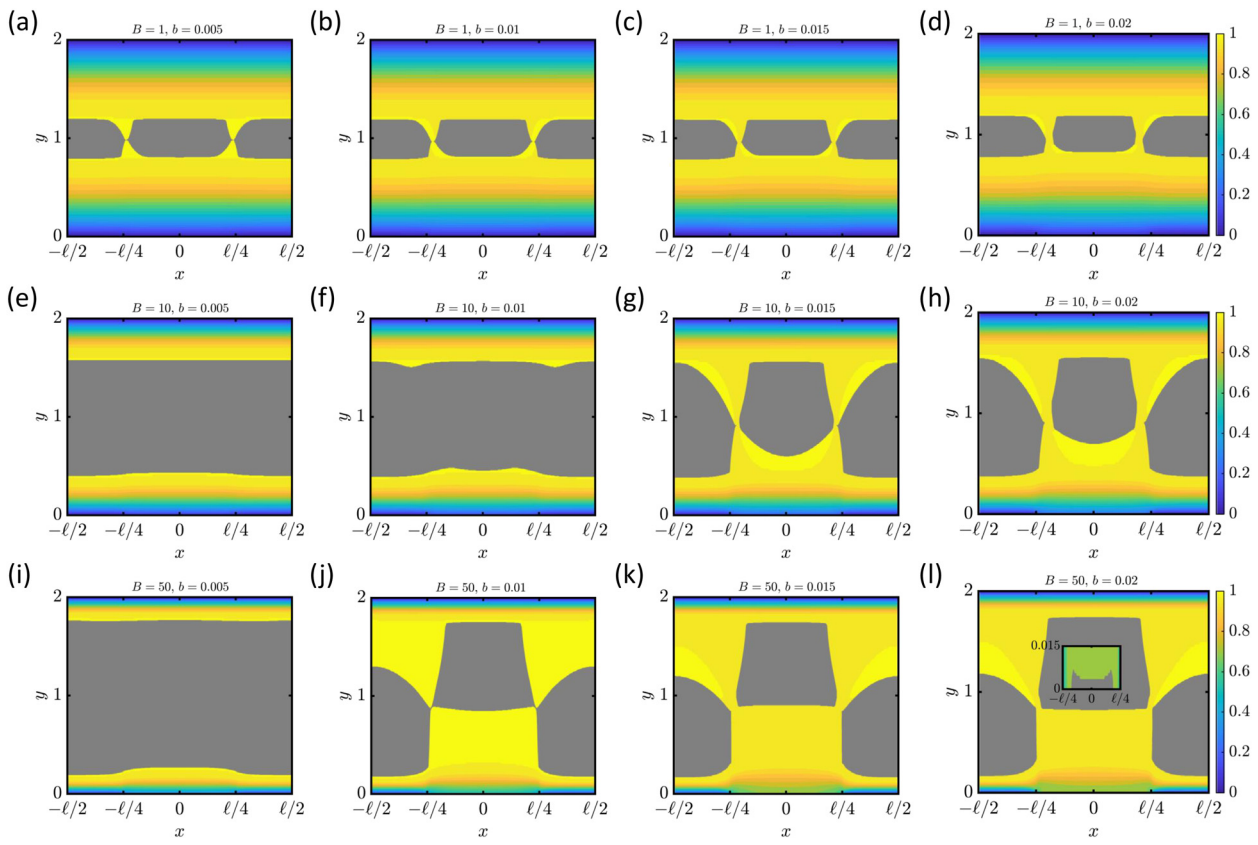

Fig. 17 Bingham fluid flowing in a channel with a superhydrophobic wall (*i.e.*, the lower wall). The liquid/air interface with partial slip condition is located at $-\ell/4 \le x \le \ell/4$ while no-slip condition is considered at $|x| > \ell/4$. The color shows the normalized streamwise velocity profile while the gray area is the unyielded region. Also, B and b are Bingham and slip number, respectively. The inset in panel l shows the SH plug on the liquid/air interface. Adapted from ref. 219 with permission from Elsevier, copyright 2023.

More recently, Joulaei *et al.*[223,224] numerically examined Poiseuille–Bingham flow with two SH walls and showed that groove misalignment strongly influences center plug deformation and breakage, suggesting relevance for drug-delivery microdevices where the unyielded plug could act as a tunable switch. They also assessed deep-learning methods (CNNs) for predicting viscoplastic flow in SH channels, concluding that with sufficient training data such AI approaches can generate effective design maps.[225] The same authors also conducted two-phase flow simulations of a Bingham fluid over a superhydrophobic surface, explicitly modeling the liquid-air interface dynamics. Their results showed that the interface remains nearly flat for deep grooves under creeping-flow conditions, whereas significant interface deformation occurs for shallow grooves and in the inertial regime. They further quantified the onset of interface depinning, which is critical for characterizing the transition from the Cassie state.[226]

In this section, we highlighted the complex slip dynamics of non-Newtonian fluids in confined systems and examined the mechanisms governing microscale slip. We also discussed emerging opportunities involving superhydrophobic surfaces, which provide new pathways for flow slippage and open applications in the transport and manipulation of complex fluids within microfluidic devices.

4.6 Yield stress and the mechanical resistance of biofilms

The mechanical integrity of biofilms plays a crucial role in their persistence across biomedical, environmental, and

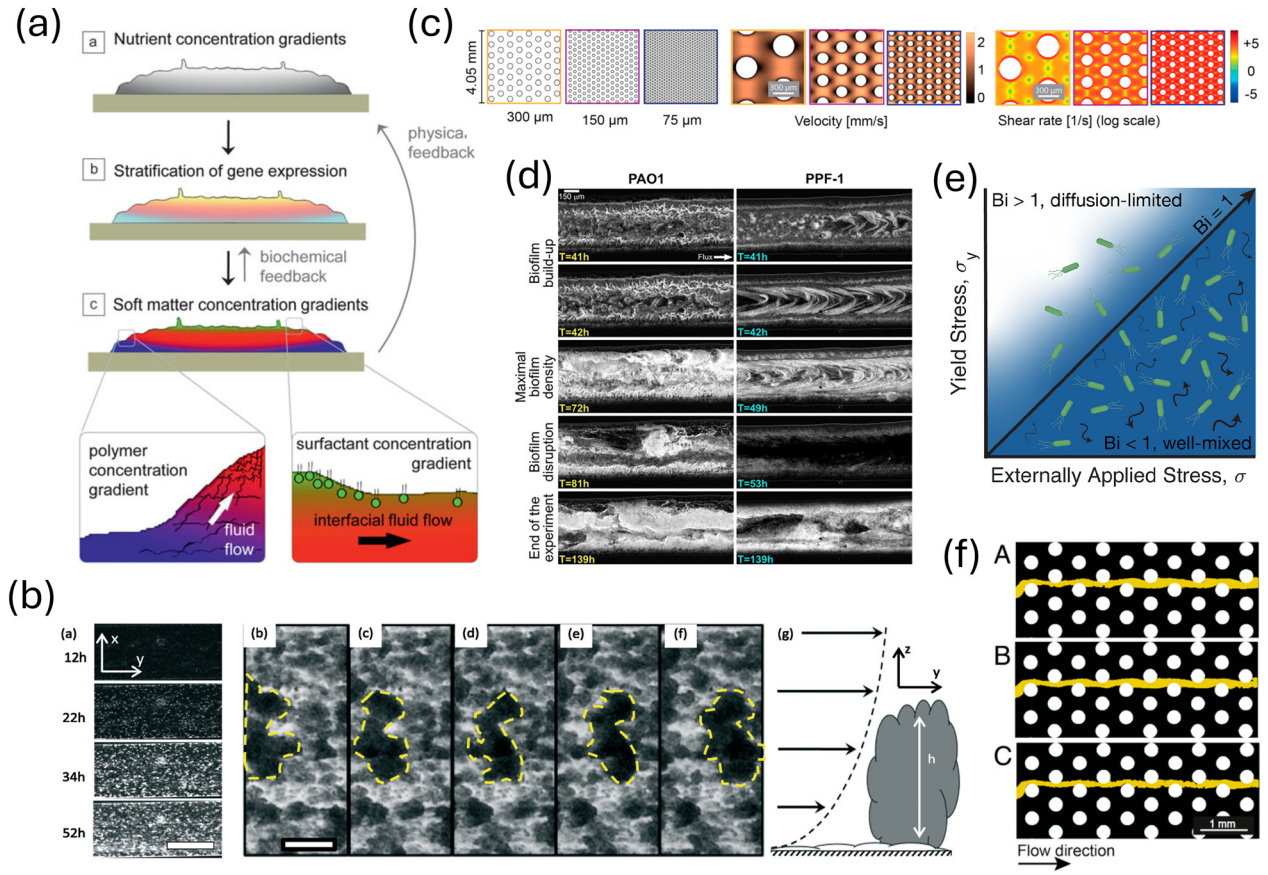

Fig. 18 (a) Coupled gradients in a model biofilm. Nutrient gradient (gray to white) forms due to consumption exceeding diffusion. Phenotypic stratification: sporulation (yellow), matrix production (pink), planktonic cells (light blue). Spatial distributions of biosurfactants (green), matrix polymers (red), colloidal cells (dark blue); heterogeneities drive internal flows, feedback on nutrient profile. Adapted from ref. 227 with permission from Springer Nature BV, copyright 2011. (b) Optical density and time-lapse micrographs of early biofilm growth under flow (0.2 mL h^{-1}, 0.1 wt% NaCl). Top view and side-view schematic show spatial growth, biofilm height, and imposed parabolic velocity profile. Scale bars: 1500 μm (top), 150 μm (micrographs). Adapted from ref. 237 with permission from Royal Society of Chemistry, copyright 2016. (c) Porous domain with three pore sizes (300, 150, 75 μm; yellow, purple, blue) and modeled velocity and shear rate fields at 1 mL h^{-1} flow. Adapted from ref. 235. (d) Biofilm development in *P. aeruginosa* strains. PAO1: mushroom-like structures (41–42 h), max density (72 h), sloughing completed (81 h), final state (139 h). PPF-1: corrugation (41–42 h), max density (49 h), sloughing (53 h), final state (139 h). Adapted from ref. 238 with permission from American Institute of Physics Publishing, copyright 2022. (e) State diagram showing how bacterial growth depends on the ratio of environmental yield stress σ_y to external stress σ. Growth is promoted in fluidized environments ($\sigma_y/\sigma < 1$) with well-mixed nutrients, and suppressed in unfluidized, diffusion-limited settings. Adapted from ref. 234 with permission from Elsevier, copyright 2024. (f) Simulated biofilm growth and PFP intermittency in a 5 × 2 mm porous domain (d = 300 μm, h = 100 μm, porosity 0.77, flow = 1 mL h^{-1}). PFPs (yellow), biofilm (black), pillars (white). Model uses yield stress 0.4 Pa. Adapted from ref. 235.

industrial settings. While biofilms are often described as viscoelastic materials, increasing experimental and theoretical evidence supports the relevance of yield stress as a defining threshold that governs biofilm deformation, detachment, and resistance to external perturbations. Indeed, biofilms can be viewed through the lens of soft matter physics, as composite materials consisting of rigid bacterial cells (colloidal phase) embedded within a hydrated, cross-linked extracellular matrix (ECM);[227] see Fig. 18a for a schematic of these spatially structured components. The ECM, primarily composed of polysaccharides, proteins, and extracellular DNA (eDNA), acts as a polymer gel that confers structural integrity. From this perspective, biofilms behave akin to yield-stress fluids, resisting deformation below a critical applied stress, with mechanical properties that can be dynamically regulated through ECM composition and hydration state.

Direct measurements of biofilm rheology have demonstrated the presence of yield stress. For example, Snowdon *et al.*[228] used parallel-plate rheometry to quantify the yield stresses of marine biofilms grown on foul-release coatings, showing that these mechanical properties correlate with biofilm cohesion and resistance to removal. Wells,[229] using oscillatory shear and tensile testing, showed that biofilms composed of alginate, eDNA, and calcium displayed distinct yield points that correlated with immune evasion; specifically, yield stress values predicted failure of phagocytosis by neutrophils. The concept of yield stress is further supported by modeling studies. Sudarsan *et al.*[230] employed an immersed boundary framework incorporating a von Mises yield criterion to simulate biofilm deformation and detachment. This approach allowed for detachment only when internal stresses exceeded a critical yield value, offering a more realistic description of sloughing than interfacial shear-based models.

Rahman *et al.*[231] and Qi & Christopher[232] have shown that biofilm mechanical behavior is highly heterogeneous and depends on ECM composition. The addition of collagen or changes in bacterial extracellular polysaccharides production can significantly increase the elastic modulus and apparent resistance to deformation. Similarly, Savorana *et al.*[233] developed a microfluidic platform to probe the nonlinear mechanical response of biofilm streamers under hydrodynamic stress, revealing complex non-Newtonian behavior. Hancock & Datta[234] demonstrated that bacterial growth in soft environments is modulated by whether applied stress surpasses the environmental yield stress, linking mechanical yielding to nutrient access and proliferation; see Fig. 18e for a stress–growth state diagram. Kurz *et al.*[235] showed that biofilm formation and disruption in porous media are governed by a competition between growth-driven expansion and shear-induced yielding, leading to intermittent clogging and recovery. This behavior was reproduced in simulations of porous domains with variable pore sizes and flow conditions (Fig. 18c and f). These findings suggest that yield stress is a relevant concept for understanding biofilm resilience, detachment, and function. Future microfluidic strategies may exploit this principle to rationally modulate biofilm behavior for therapeutic, diagnostic, and industrial applications.

Microfluidic platforms have greatly advanced biofilm rheology by uncovering time- and space-dependent mechanical behaviors that span solid-like resistance and viscous flow. Greener *et al.*[236] used passive microrheology in a microfluidic device to show that the mechanical properties of biofilms evolve during maturation, revealing spatial heterogeneity and time-dependent stiffening consistent with dynamic biofilm remodeling. Paquet-Mercier *et al.*[237] used green fluorescent protein-tagged *Pseudomonas aeruginosa* in microfluidic channels to identify a "grow and flow" phase, during which biofilms exhibited rapid front advancement and biomass trailing; see Fig. 18b for representative growth images and flow profile. Image-based tracking revealed strain rate changes associated with this transition. Increasing NaCl concentration (0–34 mM) significantly hastened the onset of this phase, suggesting sensitivity of biofilm dynamics to ionic strength. Greener[238] showed that *P. aeruginosa* biofilms from a dental unit isolate slough continuously under low shear stress (~1.4 Pa), but exhibit viscoplastic, catastrophic detachment at higher stress (~5.4 Pa) when exposed to Mg^{2+}; see time-series development in Fig. 18d. These and similar studies demonstrate that biofilm rheology evolves significantly during maturation, governed by environmental cues and spatial heterogeneity, with viscosity shifts and flow-induced deformation serving as reliable proxies for yield behavior and detachment thresholds in confined microscale environments.

4.7 Microrheological perspectives on yield stress behavior

Microrheology has emerged as a powerful approach to investigate the local mechanical behavior of complex fluids and soft materials, particularly in confined microscale environments where traditional bulk rheometry fails to capture spatial heterogeneities or stress localization. Both passive and active microrheological techniques have been leveraged to interrogate the onset of yielding, linking microscale probe dynamics to macroscopic yield stress.

A contribution by Mohan *et al.*[239] employed active microrheology to explore yielding in soft particle glasses, revealing that probe-induced displacements exhibit a sharp transition when the applied force exceeds a critical threshold, in agreement with the macroscopic yield stress. Their study showed that microviscosity inferred from probe dynamics correlates with shear-thinning trends observed in bulk, supporting the idea that yielding reflects a cage-breaking process at the microscopic level. Mutneja and Schweizer[240] presented a microscopic theory explaining how dense attractive colloidal suspensions exhibit plastic flow, single, or double yielding under shear. Double yielding emerges from a competition between bond breakage and cage disruption, with transitions governed by attraction strength, range, shear

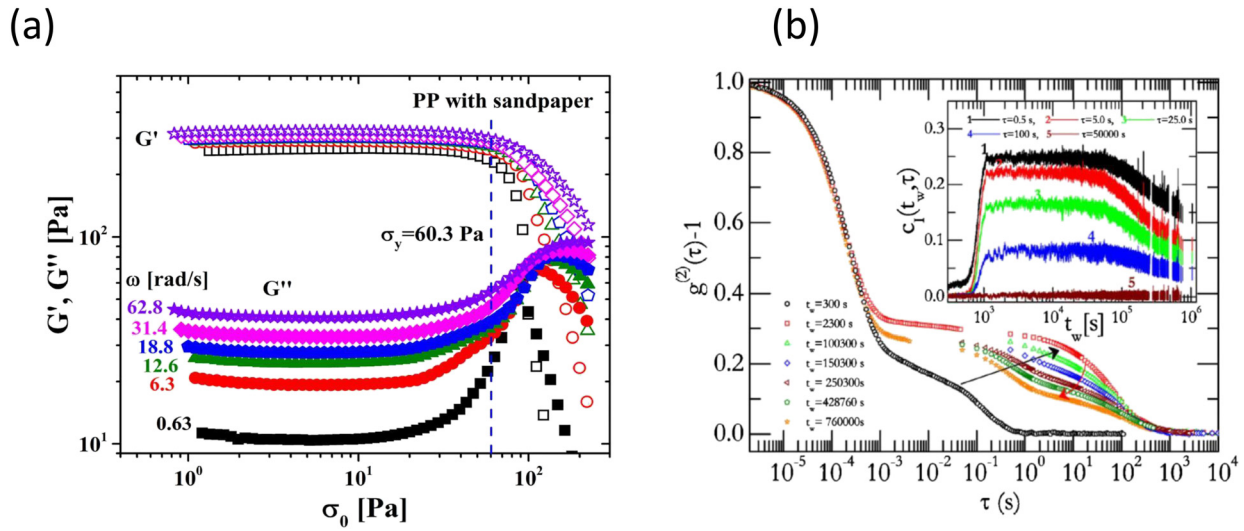

Fig. 19 (a) G' and G'' *vs.* stress for microgels under no-slip conditions across frequencies. Adapted from ref. 212 with permission from The Society of Rheology, copyright 2024. (b) Ageing and crystallization dynamics of star polymer solution with temporal correlation inset. Adapted from ref. 255 with permission from American Physical Society, copyright 2010.

rate, and packing fraction. The predictions aligned with experimental observations of attractive glasses. Ahuja *et al.*[241] discussed microstructural details and reviewed experimental systems exhibiting double yielding, highlighting similarities and differences. In particular, they examined how the continuous phase, particle properties (size, shape, softness, surface charge), and external fields (electric, magnetic, thermal, shear) affect two-step yielding. The role of local plasticity and structural rearrangement was further examined by Vitali *et al.*,[242] who developed an optofluidic microrheometer with sub-nN force sensitivity to probe local plasticity and structural rearrangement in soft microgels. Through microscale creep and recovery tests, they identified the yield onset and linear viscoelastic limits, confirming consistency with bulk rheology while revealing pre-yield intermittent dynamics and spatial heterogeneity unique to the microscale. Similarly, Medina-Bañuelos *et al.*[212] showed that wall slip in yield-stress microgels distorts oscillatory shear measurements, especially at low frequencies. Using Rheo-PIV, the authors revealed a critical slip stress below the yield point where slip causes phase shifts and waveform asymmetries, making rheometer strain measurements inaccurate and corrections unreliable; the associated stress-dependent moduli under no-slip conditions are shown in Fig. 19a. Generally speaking, wall slip can bias low shear-rate measurements, including under steady (continuous) shear.[243,244]

Other microrheological approaches have also proven instrumental in resolving variations in yield behavior. Jofore *et al.*[245] showed that, under microscale confinement, Carbopol microgels exhibit delayed yielding, slip governed by elastohydrodynamic lubrication, and direct frictional

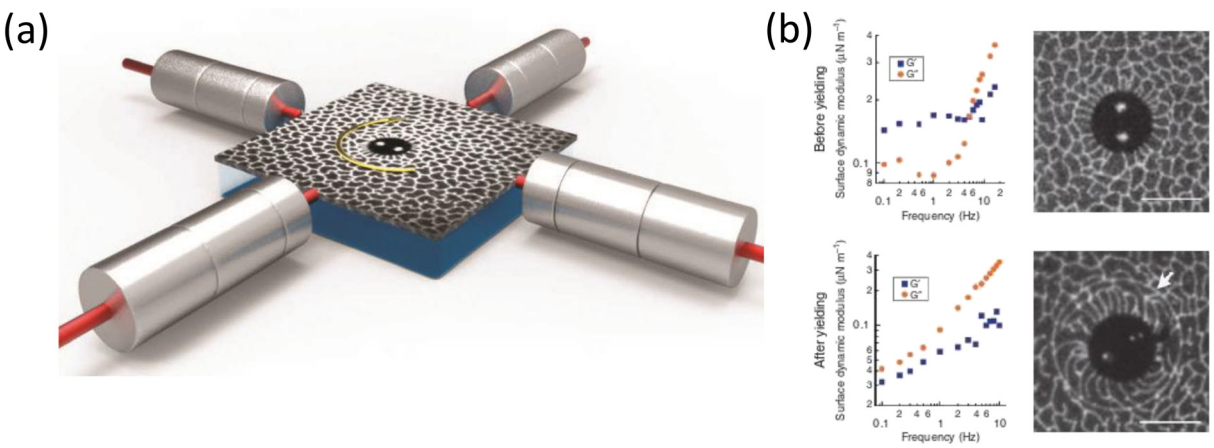

Fig. 20 (a) Ferromagnetic microbutton probe for interfacial microrheology at air–water monolayers. (b) History-dependent viscoelasticity in LC-DPPC monolayers: $G_s' > G_s''$ at low frequency, reversed after microbutton-induced reorganization and slip-line formation. Adapted from ref. 250 with permission from Springer Nature, copyright 2011.

interactions at high compression, with behavior strongly influenced by surface roughness and quantified *via* microgap rheometry. Also, we should highlight that such delayed yielding is not specific to confined flows; it has also been reported for Carbopol in conventional rheometry experiments.[246] In their review article, Joshi *et al.*[247] explored how soft glassy materials exhibit yield stress due to microscopic structural arrest and undergo physical ageing, leading to time-dependent rheological behavior (Fig. 19b). Their work highlights the interplay between ageing and deformation-induced rejuvenation, showing how stress, flow history, and microstructure govern thixotropy and viscoelastic properties across various systems like colloidal glasses, gels, and emulsions. Vleminckx and Clasen[248] reviewed non-optical microrheology techniques such as piezo-vibrators and sliding plate setups, highlighting their capability to probe yield transitions under high shear and in constrained geometries. Loosli *et al.*[249] presented a microrheology method using magnetic wire rotation to distinguish viscoelastic liquids from soft solids. In soft solids, wires showed zero average rotation across frequencies, unlike in liquids. Constitutive models were developed and validated using gellan gum gels, allowing accurate measurement of elastic moduli at ultra-low stresses. Choi *et al.*[250] developed a microrheology method that simultaneously measures and visualizes the shear response of phospholipid monolayers. They revealed that even simple lipid films exhibit viscoelasticity, yield stress, and slow recovery due to cooperative deformation of liquid-crystalline domains (Fig. 20a and b). Graphics of Carbopol gel microstructure are presented and discussed by Géraud *et al.*[251] and Jaworski *et al.*[252]

Many microrheological investigations converge on a unifying perspective: yield stress behavior is not merely a bulk-averaged threshold. In fact, they reveal that yielding and fluidization occur through localized, intermittent rearrangements and spatially heterogeneous dynamics, rather than a uniform transition.[239,242,247,253] In jammed and soft-glassy materials, each local plastic event redistributes stress through the surrounding elastic network, so nearby regions are affected over a finite cooperativity length; this is the physical origin of nonlocality in confined or strongly inhomogeneous flows.[204,206] Nonlocal constitutive models capture this by supplementing a bulk flow law with a field variable (commonly the fluidity $f \sim \dot{\gamma}/\sigma$, interpreted as a proxy for plastic activity) that is spatially coupled, for example through a diffusion-like term that allows fluidity to penetrate into nominally unyielded zones.[205,254] In this way, microrheology provides local measurements (or proxies) of $f(\mathbf{x}, t)$ and its transients, while the nonlocal model uses these data to calibrate the cooperativity length and to predict geometry-dependent velocity profiles and transient banding/front propagation.[207] By enabling high-resolution force application and displacement tracking, microrheology offers a window into the early stages of yielding, heterogeneous plasticity, and the role of microstructural architecture, *i.e.*, features critical for understanding confined flow in LOC and biological contexts.

Recent developments in microscale rheometry have enabled localized quantification of yield-stress rheology in microfluidic environments. Bubble-based techniques are particularly powerful in this context. Song *et al.*[256] used a bubble rheometer to reveal that dilute cellulose fiber gels exhibit microscale yield stresses exceeding bulk values due to structural heterogeneity. Recently, based on a novel application of single-beam acoustical tweezers, Penneron *et al.*[257] employed acoustically trapped microbubbles to measure local shear modulus in hydrogels, achieving strong agreement with bulk rheometry while offering superior depth penetration and force resolution over optical methods. The

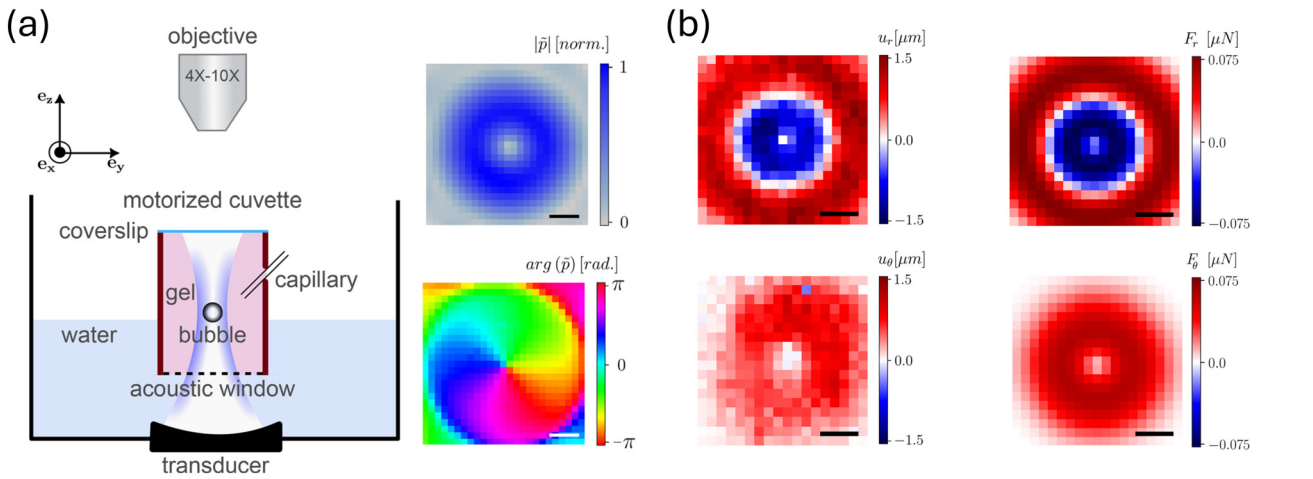

Fig. 21 (a) Experimental setup for acoustical tweezers-based microrheology, using a focused vortex beam from a piezoelectric transducer array to trap microbubbles in a hydrogel-filled cuvette for optical displacement tracking. (b) Radial (u_r) and azimuthal (u_θ) displacement fields of a microbubble (a = 80 μm) under acoustic excitation (p = 110 kPa), revealing restoring and tangential forces used to extract local shear modulus. Scale bars: 300 μm. Adapted from ref. 257 with permission from American Institute of Physics Publishing, copyright 2025.

experimental setup and representative displacement field measurements used to extract viscoelastic moduli are shown in Fig. 21. Saint-Michel and Garbin[258] analyzed acoustically driven bubble oscillations in Carbopol, showing that despite satisfying yielding criteria, strong elasticity prevents irreversible motion. Instead, bubbles undergo shape instabilities, captured across a range of mode numbers, that diverge from Kelvin–Voigt predictions (see Fig. 22). Estrada *et al.*[259] introduced inertial microcavitation rheometry, a laser-induced cavitation method that captures high strain-rate viscoelasticity (up to 10^8 s^{-1}) in soft gels. Gibaud *et al.*[260] demonstrated that ultrasonic forcing can soften colloidal gels, lower their yield stress, and accelerate fluidization *via* microcrack formation. Iwata *et al.*[261] showed that oscillatory pressure can drastically increase bubble rise in shear-thinning fluids by locally reducing viscosity, *i.e.*, an effect absent in Newtonian media. Collectively, these studies use microbubbles (and, more broadly, bubble growth/oscillation dynamics) as localized rheological perturbations that both probe and sometimes tune yielding and viscoelastic response at the relevant microscale; where confinement, heterogeneity, and rate effects can decouple local behavior from bulk flow curves. Bubble expansion can generate controlled strain fields that reveal stress-induced microstructural reorganization and spatially heterogeneous yielding pathways in fibrous gels,[256] while acoustically trapped microbubbles extend this idea into an active microrheology modality that infers local shear elasticity *in situ*.[257] These methods establish a versatile microrheological toolkit for probing local yielding, viscoelasticity, and heterogeneity in complex fluids under microfluidic confinement.

Capillary slit devices enabled shear viscosity measurements, while cross-slot stagnation flows and contraction–expansion geometries were used to probe extensional properties.[141] Considering extensional rheology, one should note that extensional kinematics are inherent to many microfluidic operations (stagnation-point regions, contractions, and necking ligaments). Therefore, extensional rheology should be treated as a primary input for yield-stress and elasto-viscoplastic materials rather than inferred from steady-shear data alone. Microfluidic stagnation-point extensional rheometry now enables controlled quantification of extensional response in relevant on-chip flow fields,[262] while recent work shows that yielding under extension can exhibit an effective extensional threshold and regime structure that are not trivially mapped from shear.[263,264] These regimes directly govern microfluidic squeezing and droplet/bubble breakup, where pinch-off is controlled by whether capillary-driven necking generates extensional stresses sufficient to overcome solid-like resistance.[265] The same considerations apply to extrusion bioprinting, in which filament continuity and shape fidelity depend on extensional thinning/breakup at the nozzle exit *versus* rapid post-deposition recovery.[266] Accordingly, microfluidic design should explicitly distinguish sub-yield extension (suppressed thinning/breakup) from yielded extensional flow (controlled thinning/pinch-off) when selecting junction/nozzle geometries and operating conditions.[262,263]

Thus, viscoelastic fluids display memory effects through stresses that depend on deformation history; however, it is now clear that yield-stress soft solids (gels, soft glasses, jammed emulsions) can also store and retrieve memory in a distinctly elasto-plastic/aging sense, because flow both (i) imprints anisotropic microstructures and residual stresses and (ii) resets the material's mechanical age, so that subsequent yielding and relaxation depend on the prior

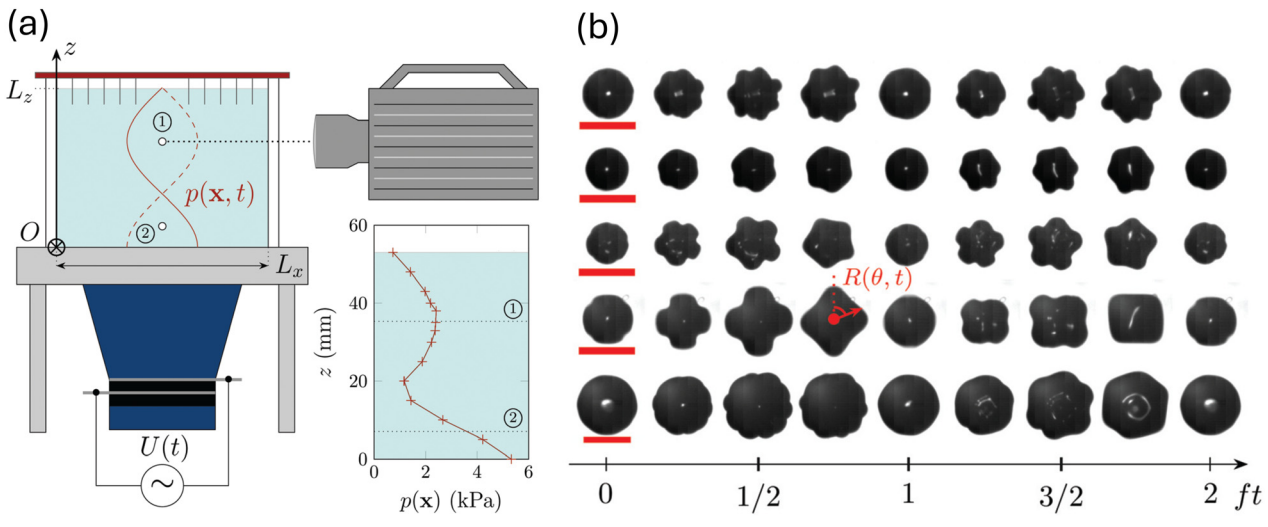

Fig. 22 (a) Experimental setup for studying microbubble dynamics in a yield-stress fluid (Carbopol) using a focused ultrasound transducer and a transparent sample chamber, enabling high-resolution optical tracking. (b) Shape oscillations of microbubbles under acoustic excitation at various frequencies over two oscillation periods. Mode numbers k = 7 to 4 are observed with decreasing frequency. These frequency- and pressure-dependent instabilities mark the transition from stable spherical oscillations to nonlinear, unpredictable dynamics. Red scale bars: 300 μm. Adapted from ref. 258 with permission from Royal Society of Chemistry, copyright 2020.

Table 3 Selected review articles on microrheology and complex fluids relevant to the present work

References	Focus and key contributions	Relevance to current review
Waigh (2005)[271]	Review of microrheological techniques, theoretical advances, and applications across polymers, colloids, and biological systems	Provides foundational overview of length-scale-dependent mechanics and tools for probing complex fluids
Weihs *et al.* (2006)[272]	Review of bio-microrheology for probing mechanical heterogeneity in live cells *via* thermal and driven particle tracking	Illustrates the role of microrheology in resolving local rheological environments within biologically complex systems
Squires & Mason (2010)[273]	Theoretical review of passive microrheology centered on the generalized Stokes–Einstein relation and its limitations	Establishes rigorous foundations and constraints for interpreting microrheological measurements in complex fluids
Rehman (2018)[274]	Review of theoretical and computational advances in passive and active microrheology, linking probe dynamics to complex fluid rheology	Clarifies how microrheology captures bulk-like non-Newtonian behavior in microscopically heterogeneous systems
Yang *et al.* (2017)[275]	Review of passive and active microrheology with emphasis on applications to complex food systems	Demonstrates relevance of microrheology to multiphase soft materials
Cicuta & Donald (2007)[276]	Introductory review of microrheological methods and their advantages over conventional rheometry	Positions microrheology as a key tool for probing soft matter and biological systems at small scales
MacKintosh & Schmidt (1999)[277]	Early overview of microrheological techniques for probing viscoelasticity at micrometer scales	Early foundational review linking microprobe-based mechanics to soft material characterization, including biological and polymeric systems
Nghe *et al.* (2011)[136]	Experimental microfluidic studies of polymer breakup, near-wall flows, shear banding, and microgel transport in complex fluids	Demonstrates how microfluidics enables access to confined flow behaviors and local rheological phenomena relevant to microrheology
Pipe & McKinley (2009)[141]	Review of microfluidic techniques for measuring bulk rheology in shear and extensional flows, including capillary and stagnation geometries	Establishes the microfluidic context for microrheological measurements and highlights flow types relevant to confined complex fluids
Waigh (2016)[278]	Update on microrheology techniques, covering instrumentation advances, statistical analysis methods, and emerging topics such as nonlinear and surface microrheology	Offers a broad methodological and application-focused foundation for interpreting microrheological data in complex and soft materials

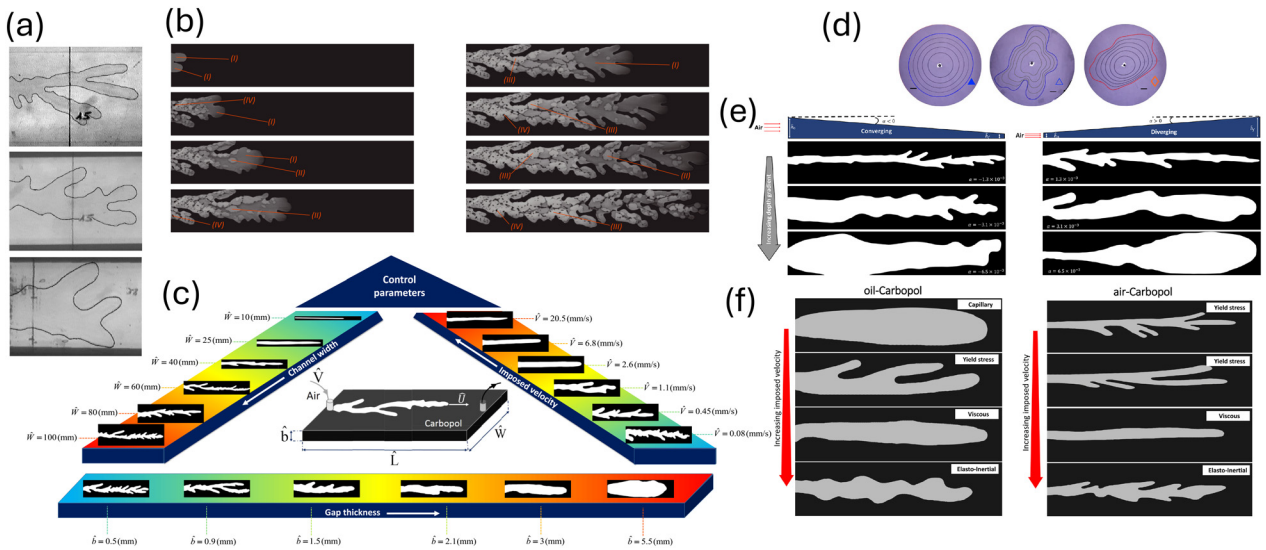

Fig. 23 (a) Viscous fingering patterns at low displacement velocities in a Hele–Shaw cell for a viscoplastic gel, with plate spacings 0.125, 0.25, and 0.75 mm (top to bottom). Adapted from ref. 279 with permission from American Physical Society, copyright 2000. (b) Image sequence showing fingering evolution in the network structure regime during viscoplastic displacement; distinct flow regions are delineated and discussed in the original study. Adapted from ref. 280 with permission from Elsevier, copyright 2017. (c) Transition from unified to ramified fingering during air–Carbopol displacement, as a function of flow parameters; central schematic shows the 3D setup, surrounding panels show 2D top-view images at low Carbopol concentration; flow is left to right. Adapted from ref. 283 with permission from American Physical Society, copyright 2020. (d) Overlaid snapshots illustrating typical interface evolution. Adapted from ref. 287. (e) Snapshots showing fingering patterns under gap gradients in converging/diverging Hele–Shaw cells; air displaces Carbopol gel. Adapted from ref. 284 with permission from American Chemical Society, copyright 2020. (f) Snapshots of Carbopol gel displaced by oil (left) and air (right) in a Hele–Shaw cell; flow is left to right. Adapted from ref. 285 with permission from Elsevier, copyright 2019.

loading path rather than only on the instantaneous stress. For instance, Sudreau *et al.* demonstrated that abrupt cessation from a presheared state can leave a history-dependent residual stress and overaged solid state, providing a direct macroscopic readout of the stored mechanical memory.[267] In addition, Chen *et al.* showed that aging gels under time-varying attractions exhibit genuine memory/state effects (including nontrivial aging trajectories) that encode the past protocol.[268] At the level of linking structure to rheology, Kamani *et al.* established an explicit connection between nanoscopic structural recorrelation and macroscopic recoverable strain under cyclic loading, and further showed that deformation memories may persist even after episodes of yielding.[269] More recently, Edera *et al.* proposed a framework tying residual stresses, directional memory, and aging to moments of a local stress distribution, and showed that near-yield training cycles can anneal (erase) stored memory—an idea that is particularly relevant for designing repeatable protocols.[270] In microfluidic contexts—where flows are intrinsically start-stop, pulsatile, strongly confined, and often driven by pressure ramps—these findings imply that apparent yielding thresholds, plug sizes, wall-slip/heterogeneity, and cycle-to-cycle device performance can be protocol dependent, so explicit conditioning (or deliberate training) should be viewed as part of device operation and microfluidic rheometry, consistent with the broader perspective on yielding pathways and open questions synthesized by Divoux *et al.*[60]

Table 3 presents a summary of microrheology studies and their relevance to this review.

4.8 Fingering instabilities in viscoplastic fluids

Relevant to our review on the behavior of yield-stress fluids in microfluidics, fingering instabilities during confined displacement flows, *i.e.*, commonly studied in Hele–Shaw cells and analogous microfluidic geometries, offer a compelling illustration of how viscoplasticity modifies classical interfacial dynamics. In microfluidic systems, where precise control over flow interfaces is essential for operations such as droplet generation, sample manipulation, or displacement of biological gels, the presence of a yield stress may lead to complex finger-like patterns that depart significantly from Newtonian behavior.

Lindner *et al.*[279] were among the first to experimentally demonstrate that fingering in yield-stress fluids displays a transition from highly branched patterns at low flow rates to more stable, unified fingers at higher velocities, as illustrated in Fig. 23a. Such flows were further analyzed by Eslami *et al.*,[280] who visualized interfacial network evolution and classified distinct flow regions (Fig. 23b). In a theoretical study, Fontana *et al.*[281] developed a weakly nonlinear mode-coupling framework for radial Hele–Shaw cells, capturing the onset of tip-splitting and side-branching events as manifestations of viscoplastic interfacial instabilities. Using inclined film flows, de Bruyn *et al.*[282] confirmed that the dominant fingering wavelength diverges near a critical inclination angle, and that both gravitational and yield stress effects play critical roles.

To systematically classify finger morphologies, Eslami and Taghavi[283] introduced modified capillary and Bond numbers (Ca*, Bo*) in rectangular geometries, delineating transitions between yield-stress-, viscosity-, and buoyancy-dominated regimes (Fig. 23c). Their earlier work also demonstrated that geometric nonuniformities, *e.g.*, converging or diverging gaps, can stabilize the interface and enhance displacement efficiency (Fig. 23e).[284] Eslami *et al.*[285] further analyzed the role of wettability and displacing fluid (air *vs.* oil) on finger morphology (Fig. 23f). Additional numerical studies by Ebrahimi *et al.*[286] have revealed the importance of rheological parameters on displacement performance and instability thresholds. Recently, Pouplard and Tsai[287] showed that radially tapered Hele–Shaw cells can passively suppress fingering in shear-thinning fluids with weak yield stress (see snapshots in Fig. 23d).

Divoux *et al.* established a quantitative onset criterion for fingering in colloidal gels based on local shear-induced yielding at the finger tip, consistent with a delayed-failure framework.[288] In addition, Palak *et al.* demonstrated that aging viscoelastic gels (*e.g.*, clay/LAPONITE® suspensions) can exhibit a rich set of interfacial morphologies during radial Hele–Shaw displacement, enabling a phase-diagram style classification in terms of elasticity/aging, flow rate, and interfacial tension,[289] and subsequently quantified the growth kinetics and spatiotemporal evolution of these patterns.[290] Finally, Parmar *et al.*, who synthesized interfacial instabilities in confined displacements of non-Newtonian fluids, explored the competing roles of capillary, viscous, elastic, and frictional mechanisms.[291]

On the other hand, the viscous fingering phenomenon was exploited to generate vessel lumens in microfluidic lab-on-a-chip devices. The viscous fingering technique was used by Tu *et al.*[292] through injecting a low viscous fluid in the unpolymerized collagen gel. The authors reported the ability to control the diameters of hollow tubes produced by viscous fingering technique through manipulation of the ambient temperature, passive pump pressure, pre-polymerization time, and the collagen concentration. Using viscous fingering approach, Delannoy *et al.*[293] managed to produce multi-layered human blood vessels-on-chip device. Injecting a low viscous fluid in a collagen solution, the authors refined this method to create blood vessels composed of two concentric and distinct layers of human endothelial and perivascular cells formed around a hollow lumen. In another work, Bischel *et al.*[294] used the viscous fingering method to develop ECM hydrogels with patterned lumens, proposing an accelerated method in generating physiologically relevant models of tissues. In addition to the classical Newtonian fingering mechanisms governed by viscous contrast and capillarity,[295] complex rheology can substantially modify instability development. A finite yield stress introduces a critical stress threshold, which can suppress deformation in

low-stress regions while concentrating flow in yielded zones; as a result, fingers may become wider and blunter. Wall slip can further influence this behavior by modifying stress transmission at the boundaries, thereby affecting finger-width selection and the transition from fingering to fracture-like patterns.[296,297] Thixotropy adds another level of complexity through a structural relaxation timescale: the observed finger width, tip-splitting behavior, and regime boundaries then depend on the competition between advection and microstructural rebuilding, leading to distinct morphology transitions as the forcing changes.[298] Finally, in jammed yield-stress materials, flow may become nonlocal, meaning that plastic activity can propagate over a finite cooperativity length. In this case, the intense shearing near the finger tip can fluidize neighboring low-stress regions, which in turn alters finger morphology and shifts transition regimes in confined microchannels.[204,254]

The aforementioned studies show that fingering in viscoplastic fluids cannot be captured by classical linear stability theory alone. Instead, the interaction between yield stress (and other rheological properties), geometry, and flow conditions governs a range of morphological behaviors highly relevant to LOC systems involving yield-stress formulations. In fact, strategic design of microchannel geometry and tuning of flow parameters provide routes for controlling interfacial stability in microfluidic applications. On the other side, the viscous fingering instability could be controlled to design LOC devices that are more physiologically relevant. Therefore, there is a two way coupling between the viscous fingering phenomenon and the microfluidic device design.

5 Summary, critical remarks and future opportunities

5.1 Summary

Through this review, we highlighted the role of fluid rheology in microfluidics, focusing on yield-stress materials while also addressing shear-thinning/thickening, viscoelasticity, and thixotropy where relevant. We began by introducing the main concepts and tools, namely constitutive models for yield-stress fluids and two categories of microfluidic devices. In section 2, we detailed the Bingham, Herschel–Bulkley, Casson, and Saramito models.

In section 3, we considered the microfluidic technology. We first reviewed two main microfluidic categories: continuous-flow, where fluid volumes traverse channels for tasks such as particle/cell separation, and droplet microfluidics, aimed at generating droplets. To illustrate continuous-flow devices, we examined CTC separation from cancer patient blood, covering methods including filtration, hydrodynamics, dielectrophoresis, and acoustics. We then discussed droplet generation, mixing, and sorting *via* T-junction, flow-focusing, and dielectrophoretic methods.

In section 4, we detailed the role of yield-stress rheology in microfluidic applications. For CTC separation, we examined how blood yield stress creates unyielded regions in low-shear zones. In bioprinting, we highlighted yield stress, shear-thinning, viscoelasticity, and thixotropy in direct ink writing and embedded printing. Electrorheological fluids were discussed with constitutive models and applications in digital control (droplet logic, pumps, valves). We then addressed microscale locomotion, emphasizing yield stress as both suppressing and enabling propulsion, and wall slip of complex fluids shaped by rheology and surface textures. ECM yield stress in biofilms was shown to govern resilience, detachment, and function. Microrheology of yield-stress materials was reviewed, stressing microfluidic approaches for confined environments where conventional rheometry fails. Finally, we analyzed viscous fingering in microfluidics, including both device design for controlling fingering and the inverse, *i.e.*, using fingering to tune design.

5.2 Critical remarks and future opportunities

Here, we critically discuss each specific application in section 4 and then highlight future research opportunities for that.

5.2.1 CTCs separation

Critical remarks. Considering the different methods developed for CTCs separation, the focus has been on optimizing the separation efficiency. Although various experimental and numerical efforts have addressed this, a renewed consideration of the complex rheological properties of blood seems necessary. In fact, the blood yield stress (caused by rouleaux formation) and viscoelasticity can strongly affect the blood flow dynamics inside the device, and this may suppress or enhance CTCs separation, depending on how the device design was inspired by blood rheology.

Future opportunities. • How low-shear regions can be manipulated and controlled to enhance CTCs separation in different microfluidic techniques: the unyielded regions due to the formation of rouleaux may have both suppressing and enhancing effects on CTCs separation.

• How device design could benefit from blood viscoelasticity in CTCs separation: blood viscoelasticity can cause elastic instabilities that might either suppress or enhance device efficiency.

• New smaller vortices (secondary flows) may emerge in spiral microfluidic devices due to blood viscoelasticity; this is a new feature for which it is unclear how it affects CTCs separation.

• In micro-vortexing methods in expansion–contraction microchannels, blood yield stress and viscoelasticity may complicate the formation of corner vortices and thus complicate CTCs separation, *i.e.*, a feature that requires more study.

5.2.2 Bioprinting

Critical remarks. In bioprinting, *i.e.*, both direct ink writing and embedded writing, the rheology of the ink is critical. Many studies have evaluated different rheological effects on the quality of ink writing. Given that many printable inks carry cells/particles, it is not clear how ink

rheology can affect cell/particle migration during the printing process. This is important since cell/particle positioning can eventually affect the quality of the printed product. On the other hand, the presence of cells/particles and their migration may affect ink rheology as well, *i.e.*, a feature that is hard to investigate.

In embedded bioprinting, it is not clear how variation in ink–bath surface tension (*i.e.*, due to surfactants) may affect the quality of printing. In addition, how might the large molecules in a yield-stress bath affect the surface properties of the formed droplet/structure? Another question concerns the rheological properties of the bath, *i.e.*, what would be the optimum values of yield stress, viscoelasticity, shear-thinning index, and thixotropy? Are we always looking for small thixotropy?

Future opportunities. • How ink rheology, *i.e.*, yield stress, viscoelasticity, shear-thinning, thixotropy, can affect cell/particle migration during printing.

• Is there any inverse effect, *i.e.*, does cell/particle migration and possible accumulation in low-shear zones affect the local rheology of the ink?

• Regarding embedded printing, what effects could surface tension and bath rheology have on the quality of printing?

5.2.3 Electrorheological fluids

Critical remarks. Although there has been much progress in developing constitutive laws for electrorheological fluids, there are still many unexplored physical aspects. For example, it is not clear how yield-stress rheology could change for different chemistries under a uniform electric field. In addition, how other rheological aspects, *e.g.*, viscoelasticity and thixotropy, could be affected by the electric field and might be controlled for specific applications.

Future opportunities. • Developing more sophisticated and comprehensive constitutive laws for electrorheological fluids.

• Quantifying the transient response to an external electric field. Could we design new devices based on transient rheological changes that are precisely predictable?

5.2.4 Locomotion in complex fluids

Critical remarks. The study of microorganism/robot locomotion in complex fluids exhibiting yield stress, viscoelasticity, shear-thinning/thickening, and thixotropy is in its early stages. Although important theories, *e.g.*, slender-body theory in yield-stress fluids, have been developed and have provided significant new understanding and insights, there is still a wide range of possibilities that could be explored. In fact, the shapes of microorganisms/robots and their modes of motion are diverse, and their combination with diverse arrays of rheological complexities opens a new area of research.

Future opportunities. • Considering simple yield-stress fluids (*i.e.*, the Bingham model), how could the developed theories be extended to more complex swimmer topologies and modes of motion?

• Considering simple shapes for the swimmer, how could the developed theories be extended to more complicated rheology, *i.e.*, highly shear-thinning/thickening properties, highly viscoelastic media, elasto-viscoplastic fluids, thixotropic/rheopectic materials, *etc.*?

• How could micro-swimmers/robots be designed to develop micro-rheometry devices?

5.2.5 Slip at micro-scale

Critical remarks. Slip of complex fluids has a long history of studies and modeling. A less explored area is the slip of complex fluids at the micro-scale, *i.e.*, the scales that are typically similar to the size of micro-molecules or to the lubrication layer near the wall. In fact, both the constitutive law and the slip mechanism of non-Newtonian and yield-stress fluids would differ at the micro-scale. Regarding superhydrophobicity-driven slip, although recent works have considered shear-thinning and viscoplastic rheology, there is still a significant dearth of understanding of complex-fluid slip over superhydrophobic surfaces at the micro-scale.

Future opportunities. • How would the interaction of micro-molecules with solid walls be affected by confinement at the micro-scale?

• How do viscoelastic, shear-thickening, elasto-viscoplastic, and thixotropic/rheopectic materials interact with superhydrophobic surfaces?

5.2.6 Biofilm mechanical resistance

Critical remarks. Biofilms resist deformation through a combined yield–elastic response: the EPS network stores elastic energy at small strain, but yields plastically once a threshold is exceeded. Most models treat them as either soft gels (elastic) or yield-stress solids (plastic), failing to capture this duality.

Future opportunities. • Develop multiscale models coupling EPS microstructure, cell density, and rheology to predict resistance under realistic microfluidic stresses.

• Establish standardized protocols for measuring yield stress (and elasticity) in biofilms, with emphasis on reproducibility across geometries and timescales.

• Incorporate elasto-viscoplastic and thixotropic constitutive laws into biofilm simulations to capture both solid-like persistence and time-dependent restructuring.

5.2.7 Microrheology

Critical remarks. Microfluidic rheometry must more clearly address complex rheology, in particular combined yield stress and nonlinear elasticity. Current approaches are fundamentally limited by sensitivity (sub-Pa stresses) and by ignoring nonlocal and slip effects that dominate at micron scales. Optical bubble oscillation as a microrheological tool resolves high-frequency moduli but the link with low- or moderate-frequency properties is missing. Also, there is no unified framework for translating microrheological measurements into practical constitutive parameters.

Future opportunities. • Develop extensional and mixed-flow microrheometers, with sufficient resolution to quantify small yield stress for practical and natural fluids.

• Integrate micro-PIV/fluorescent velocimetry with inverse modeling to directly map stress fields and yield surfaces in confined microflows.

• Establish theoretical bridges between active and passive microrheology that account for confinement and slip, rather than just extrapolating bulk laws.

5.2.8 Viscous fingering

Critical remarks. Current models rarely incorporate elasto-viscoplastic constitutive laws, making it difficult to capture the observed transitions between stable, screened, or branching fingers across large parameter ranges. Experiments remain largely two-dimensional, neglecting how microchannel depth and aspect ratio control confinement and stress localization.

Future opportunities. • Formulate scaling laws based on thixo-elasto-viscoplastic rheology, incorporating yield number, Deborah number, and thixotropy time scales, to map fingering regimes.

• Extend viscous fingering studies into true 3D microchannels with controlled roughness and wettability, to mimic porous media transport at the microscale.

• Translate fingering into a design principle for patterning and templating in microfludic systems.

Author contributions

All authors jointly conceived, developed, and wrote the manuscript.

Conflicts of interest

There are no conflicts to declare.

Data availability

No primary research results, software or code have been included and no new data were generated or analyzed as part of this review.

Acknowledgements

We appreciate the invitation to submit this manuscript to *Lab on a Chip*. We acknowledge support from the Canada Research Chair (CRC) in Modeling Complex Flows (Grant No. CG125810) and the Natural Sciences and Engineering Research Council of Canada (NSERC, Discovery Grant No. CG109154). Use of grammar/language tools is acknowledged to improve text readibility. HR also gratefully acknowledges support from NSERC and the Government of Canada's Tri-agency through the Banting Postdoctoral Fellowship (Funding Reference No. BPF-204250).

References

1 H. Pei, L. Li, Z. Han, Y. Wang and B. Tang, *Lab Chip*, 2020, 3854–3875.
2 G. Whitesides, *Nature*, 2006, **442**, 368–373.
3 H. Stone, A. Stroock and A. Ajdari, *Annu. Rev. Fluid Mech.*, 2004, **36**, 381–411.
4 T. Squires and S. Quake, *Rev. Mod. Phys.*, 2005, **77**(3), 977–1026.
5 N. Nguyen, S. Wereley and S. Shaegh, *Fundamentals and applications of microfluidics*, Artech House, 2019.
6 D. Weibel and G. Whitesides, *Curr. Opin. Chem. Biol.*, 2006, **10**, 584–591.
7 Y. Ding, P. Howes and A. deMello, *Anal. Chem.*, 2019, **92**, 132–149.
8 N. J. Balmforth, I. Frigaard and G. Ovarlez, *Annu. Rev. Fluid Mech.*, 2014, **46**, 121–146.
9 D. Bonn, M. M. Denn, L. Berthier, T. Divoux and S. Manneville, *Rev. Mod. Phys.*, 2017, **89**, 035005.
10 T. A. Burinaru, M. Avram, A. Avram and C. Marculescu, *ACS Comb. Sci.*, 2018, **20**, 107–126.
11 V. Sharma, A. Jaishankar, Y. C. Wang and G. H. McKinley, *Soft Matter*, 2011, **7**, 5150–5160.
12 T. Matsumoto and H. Inoue, *Chem. Phys.*, 1993, **178**, 591–598.
13 R. Thompson, L. Sica and P. de Souza Mendes, *J. Non-Newtonian Fluid Mech.*, 2018, **261**, 211–219.
14 R. Larson and Y. Wei, *J. Rheol.*, 2019, **63**, 477–501.
15 R. B. Bird, R. C. Armstrong and O. Hassager, *Dynamics of polymeric liquids. Vol. 1: Fluid mechanics*, John Wiley and Sons Inc., New York, NY, 1986.
16 A. Gusev and T. Bernhard, *Macromolecules*, 2024, **57**, 10152–10163.
17 R. Larson, *The structure and rheology of complex fluids*, Oxford University Press, 1999.
18 I. Morrison, in *Dispersions*, John Wiley and Sons, Ltd, 2003.
19 G. Ovarlez, L. Tocquer, F. Bertrand and P. Coussot, *Soft Matter*, 2013, **9**, 5540–5549.
20 N. S. And and D. De Kee, *Can. J. Chem. Eng.*, 2001, **79**, 36–41.
21 H. Inoue and T. Matsumoto, *J. Rheol.*, 1994, **38**, 973–984.
22 S. Ikeda and K. Nishinari, *Biomacromolecules*, 2000, **1**, 757–763.
23 J. Horner, M. Armstrong, N. Wagner and A. Beris, *J. Rheol.*, 2018, **62**, 577–591.
24 O. Baskurt and H. Meiselman, *Seminars in Thrombosis and Hemostasis*, 2024, pp. 902–915.
25 R. Mehri, C. Mavriplis and M. Fenech, *PLoS One*, 2018, **13**, e0199911.
26 O. Korculanin, T. Kochetkova and M. Lettinga, *Front. Phys.*, 2021, **9**, 721368.
27 Z. Varga, V. Grenard, S. Pecorario, N. Taberlet, V. Dolique, S. Manneville, T. Divoux, G. McKinley and J. Swan, *Proc. Natl. Acad. Sci. U. S. A.*, 2019, **116**, 12193–12198.
28 S. Lai, Y. Wang, D. Wirtz and J. Hanes, *Adv. Drug Delivery Rev.*, 2009, **61**, 86–100.
29 D. Thornton and J. Sheehan, *Proc. Am. Thorac. Soc.*, 2004, **1**, 54–61.
30 M. Jory, D. Donnarumma, C. Blanc, K. Bellouma, A. Fort, I. Vachier, L. Casanellas, A. Bourdin and G. Massiera, *Interface Focus*, 2022, **12**, 20220028.
31 J. Fahy and B. Dickey, *N. Engl. J. Med.*, 2010, **363**, 2233–2247.
32 C. Schaefer, G. McKinley and T. McLeish, *Theme issue on complex rheology in biological systems*, 2022.
33 S. Geisel, E. Secchi and J. Vermant, *Interface Focus*, 2022, **12**, 20220032.

34 P. Stoodley, R. Cargo, C. Rupp, S. Wilson and I. Klapper, *J. Ind. Microbiol. Biotechnol.*, 2002, **29**, 361–367.
35 I. Klapper, C. Rupp, R. Cargo, B. Purvedorj and P. Stoodley, *Biotechnol. Bioeng.*, 2002, **80**, 289–296.
36 H. Flemming and J. Wingender, *Nat. Rev. Microbiol.*, 2010, **8**, 623–633.
37 S. Fabbri and P. Stoodley, *The perfect slime–microbial extracellular polymeric substances*, 2016, pp. 153–178.
38 R. Donlan, *Emerging Infect. Dis.*, 2002, **8**, 881.
39 P. Coussot, *J. Non-Newtonian Fluid Mech.*, 2014, **211**, 31–49.
40 P. de Souza Mendes and R. Thompson, *J. Non-Newtonian Fluid Mech.*, 2012, **187**, 8–15.
41 R. Ewoldt and G. McKinley, *Rheol. Acta*, 2017, **56**, 195–210.
42 D. Fraggedakis, Y. Dimakopoulos and J. Tsamopoulos, *J. Non-Newtonian Fluid Mech.*, 2016, **236**, 104–122.
43 I. Frigaard, *Curr. Opin. Colloid Interface Sci.*, 2019, **43**, 80–93.
44 M. Piau and J. Piau, *J. Non-Newtonian Fluid Mech.*, 2007, **144**, 59–72.
45 P. Saramito and A. Wachs, *Rheol. Acta*, 2017, **56**, 211–230.
46 N. J. Balmforth, I. A. Frigaard and G. Ovarlez, *Annu. Rev. Fluid Mech.*, 2014, **46**, 121–146.
47 N. Dubash and I. Frigaard, *J. Non-Newtonian Fluid Mech.*, 2007, **142**, 123–134.
48 A. Beris, J. Tsamopoulos, R. Armstrong and R. Brown, *J. Fluid Mech.*, 1985, **158**, 219–244.
49 Z. Varga and J. Swan, *J. Rheol.*, 2018, **62**, 405–418.
50 S. Jamali, R. Armstrong and G. McKinley, *Mater. Today Adv.*, 2020, **5**, 100026.
51 N. Casson, *Rheology of Disperse Systems*, 1959.
52 G. R. Cokelet, E. Merrill, E. Gilliland, H. Shin, A. Britten and R. Wells Jr, *Trans. Soc. Rheol.*, 1963, **7**, 303–317.
53 S. Chien, S. Usami, H. M. Taylor, J. L. Lundberg and M. I. Gregersen, *J. Appl. Physiol.*, 1966, **21**, 81–87.
54 E. Errill, *Physiol. Rev.*, 1969, **49**, 863–888.
55 C. L. Morris, D. L. Rucknagel, R. Shukla, R. A. Gruppo, C. M. Smith II and P. Blackshear Jr, *Microvasc. Res.*, 1989, **37**, 323–338.
56 H. Meiselman, E. Merrill, E. Salzman, E. Gilliland and G. Pelletier, *J. Appl. Physiol.*, 1967, **22**, 480–486.
57 E. W. Merrill and G. A. Pelletier, *J. Appl. Physiol.*, 1967, **23**, 178–182.
58 P. Møller, J. Mewis and D. Bonn, *Soft Matter*, 2006, **2**, 274–283.
59 P. Moller, A. Fall, V. Chikkadi, D. Derks and D. Bonn, *Philos. Trans. R. Soc., A*, 2009, **367**, 5139–5155.
60 T. Divoux, *et al.*, *Soft Matter*, 2024, **20**, 6868–6888.
61 M. Larsson, J. Duffy and A. B. Min, *Annu. Trans. - Nord. Rheol. Soc.*, 2013, **21**, 125–138.
62 M. Dinkgreve, J. Paredes, M. Denn and D. Bonn, *J. Non-Newtonian Fluid Mech.*, 2016, **238**, 233–241.
63 S. Dhar, T. Liberto, C. Barentin, T. Divoux and A. Robisson, *Rheol. Acta*, 2024, **63**, 657–672.
64 D. Kavishvar and A. Ramachandran, *Adv. Colloid Interface Sci.*, 2023, **322**, 103049.
65 D. Kavishvar and A. Ramachandran, *Lab Chip*, 2024, **24**, 3135–3148.
66 D. De Kee, *Phys. Fluids*, 2021, **33**, 111301.
67 P. Saramito, *J. Non-Newtonian Fluid Mech.*, 2007, **145**, 1–14.
68 J. Oldroyd, *Proc. R. Soc. London, Ser. A*, 1950, **200**, 523–541.
69 J. Hinch and O. Harlen, *J. Non-Newtonian Fluid Mech.*, 2021, **298**, 104668.
70 R. Agrawal, E. García-Tuñón, R. J. Poole and C. P. Fonte, *J. Non-Newtonian Fluid Mech.*, 2025, **338**, 105407.
71 M. Caggioni, V. Trappe and P. Spicer, *J. Rheol.*, 2020, **64**, 413–422.
72 K. Kamani, G. Donley and S. Rogers, *Phys. Rev. Lett.*, 2021, **126**, 218002.
73 G. Thompson, J. Lee, K. Kamani, N. Flores-Velasco, S. Rogers and B. Harley, *Adv. Mater.*, 2025, **37**, 2503635.
74 S. Jamali, E. Del Gado and J. Morris, *J. Rheol.*, 2020, **64**, 1501–1524.
75 F. Bragheri, R. M. Vázquez and R. Osellame, *Three-Dimensional Microfabrication Using Two-Photon Polymerization*, Elsevier, 2020, pp. 493–526.
76 M. J. Jebrail, M. S. Bartsch and K. D. Patel, *Lab Chip*, 2012, **12**, 2452–2463.
77 R. Sista, Z. Hua, P. Thwar, A. Sudarsan, V. Srinivasan, A. Eckhardt, M. Pollack and V. Pamula, *Lab Chip*, 2008, **8**, 2091–2104.
78 V. Srinivasan, V. K. Pamula and R. B. Fair, *Lab Chip*, 2004, **4**, 310–315.
79 J. D. Caplin, N. G. Granados, M. R. James, R. Montazami and N. Hashemi, *Adv. Healthcare Mater.*, 2015, **4**, 1426–1450.
80 C. W. Yung, J. Fiering, A. J. Mueller and D. E. Ingber, *Lab Chip*, 2009, **9**, 1171–1177.
81 N. Bhise, J. Ribas, V. Manoharan, Y. Zhang, A. Polini, S. Massa, M. Dokmeci and A. Khademhosseini, *J. Controlled Release*, 2014, **190**, 82–93.
82 K. Chen, P. Dopico, J. Varillas, J. Zhang, T. J. George and Z. H. Fan, *Angew. Chem., Int. Ed.*, 2019, **58**, 7606–7610.
83 X. Qin, S. Park, S. Duffy, K. Matthews, R. Ang, T. Todenhöfer, H. Abdi, A. Azad, J. Bazov and K. Chi, *et al.*, *Lab Chip*, 2015, **15**, 2278–2286.
84 L. Huang, E. Cox, R. Austin and J. Sturm, *Science*, 2004, **304**, 987–990.
85 M. Ahmed, M. Abate, Y. Song, Z. Zhu, F. Yan, Y. Xu, X. Wang, Q. Li and C. Yang, *Angew. Chem., Int. Ed.*, 2017, **56**, 10681–10685.
86 H. Hou, M. Warkiani, B. Khoo, Z. Li, R. Soo, D. Tan, W. Lim, J. Han, A. Bhagat and C. Lim, *Sci. Rep.*, 2013, **3**, 1259.
87 M. Warkiani, B. Khoo, L. Wu, A. Tay, A. Bhagat, J. Han and C. Lim, *Nat. Protoc.*, 2016, **11**, 134–148.
88 M. Dhar, J. Lam, T. Walser, S. Dubinett, M. Rettig and D. Di Carlo, *Proc. Natl. Acad. Sci. U. S. A.*, 2018, **115**, 9986–9991.
89 S. Shim, K. Stemke-Hale, A. Tsimberidou, J. Noshari, T. Anderson and P. Gascoyne, *Biomicrofluidics*, 2013, **7**(1), 011807.
90 M. Sun, J. Xu, J. Shamul, X. Lu, S. Husain and X. He, *Biomaterials*, 2019, **197**, 161–170.

91 C. Magnusson, P. Augustsson, A. Lenshof, Y. Ceder, T. Laurell and H. Lilja, *Anal. Chem.*, 2017, **89**, 11954–11961.
92 S. Karthick, P. Pradeep, P. Kanchana and A. Sen, *Lab Chip*, 2018, **18**, 3802–3813.
93 H. Cho, J. Kim, H. Song, K. Y. Sohn, M. Jeon and K.-H. Han, *Analyst*, 2018, **143**, 2936–2970.
94 J. Mong and M.-H. Tan, *Trends Biotechnol.*, 2018, **36**, 511–522.
95 A. F. Sarioglu, N. Aceto, N. Kojic, M. C. Donaldson, M. Zeinali, B. Hamza, A. Engstrom, H. Zhu, T. K. Sundaresan and D. T. Miyamoto, *et al.*, *Nat. Methods*, 2015, **12**, 685–691.
96 K. Loutherback, J. D'Silva, L. Liu, A. Wu, R. Austin and J. Sturm, *AIP Adv.*, 2012, **2**, 042107.
97 M. E. Warkiani, G. Guan, K. B. Luan, W. C. Lee, A. A. S. Bhagat, P. K. Chaudhuri, D. S.-W. Tan, W. T. Lim, S. C. Lee and P. C. Chen, *et al.*, *Lab Chip*, 2014, **14**, 128–137.
98 J. Sun, M. Li, C. Liu, Y. Zhang, D. Liu, W. Liu, G. Hu and X. Jiang, *Lab Chip*, 2012, **12**, 3952–3960.
99 J. Sun, C. Liu, M. Li, J. Wang, Y. Xianyu, G. Hu and X. Jiang, *Biomicrofluidics*, 2013, **7**, 011802.
100 S. C. Hur, A. J. Mach and D. Di Carlo, *Biomicrofluidics*, 2011, **5**, 022206.
101 E. Sollier, D. E. Go, J. Che, D. R. Gossett, S. O'Byrne, W. M. Weaver, N. Kummer, M. Rettig, J. Goldman and N. Nickols, *et al.*, *Lab Chip*, 2014, **14**, 63–77.
102 N. Xiang, J. Wang, Q. Li, Y. Han, D. Huang and Z. Ni, *Anal. Chem.*, 2019, **91**, 10328–10334.
103 Y. Zhao, X. Zhang, J. Bai, H. Jia, M. Chen and J. Wang, *Anal. Chem.*, 2024, **96**, 18187–18194.
104 A. Abdulla, W. Liu, A. Gholamipour-Shirazi, J. Sun and X. Ding, *Anal. Chem.*, 2018, **90**, 4397–4405.
105 L. Y. Yeo and J. R. Friend, *Annu. Rev. Fluid Mech.*, 2014, **46**, 379–406.
106 P. Augustsson, C. Magnusson, M. Nordin, H. Lilja and T. Laurell, *Anal. Chem.*, 2012, **84**, 7954–7962.
107 M. Antfolk, C. Antfolk, H. Lilja, T. Laurell and P. Augustsson, *Lab Chip*, 2015, **15**, 2102–2109.
108 T. Thorsen, R. Roberts, F. Arnold and S. Quake, *Phys. Rev. Lett.*, 2001, **86**, 4163.
109 A. Utada, E. Lorenceau, D. Link, P. Kaplan, H. Stone and D. Weitz, *Science*, 2005, **308**, 537–541.
110 R. Ahmed and T. Jones, *J. Electrost.*, 2006, **64**, 543–549.
111 M. Pollack, A. Shenderov and R. Fair, *Lab Chip*, 2002, **2**, 96–101.
112 S.-Y. Teh, R. Lin, L.-H. Hung and A. P. Lee, *Lab Chip*, 2008, **8**, 198–220.
113 L. Yobas, S. Martens, W. Ong and N. Ranganathan, *Lab Chip*, 2006, **6**, 1073–1079.
114 M. Bringer, C. Gerdts, H. Song, J. Tice and R. Ismagilov, *Philos. Trans. R. Soc., A*, 2004, **362**, 1087–1104.
115 J. Atencia and D. J. Beebe, *Nature*, 2005, **437**, 648–655.
116 N. L. Jeon, H. Baskaran, S. K. Dertinger, G. M. Whitesides, L. Van De Water and M. Toner, *Nat. Biotechnol.*, 2002, **20**, 826–830.
117 I. Kobayashi, K. Uemura and M. Nakajima, *Colloids Surf., A*, 2007, **296**, 285–289.
118 R. B. Fair, *Microfluid. Nanofluid.*, 2007, **3**, 245–281.
119 M. J. Fuerstman, P. Garstecki and G. M. Whitesides, *Science*, 2007, **315**, 828–832.
120 T. Nisisako, S. Okushima and T. Torii, *Soft Matter*, 2005, **1**, 23–27.
121 J. Xu, S. Li, Y. Wang and G. Luo, *Appl. Phys. Lett.*, 2006, **88**, 133506.
122 J. Xu, S. Li, J. Tan, Y. Wang and G. Luo, *AIChE J.*, 2006, **52**, 3005–3010.
123 S. L. Anna, N. Bontoux and H. A. Stone, *Appl. Phys. Lett.*, 2003, **82**, 364–366.
124 C. Zhou, P. Yue and J. J. Feng, *Phys. Fluids*, 2006, **18**, 092105.
125 S. K. Cho, H. Moon and C.-J. Kim, *J. Microelectromech. Syst.*, 2003, **12**, 70–80.
126 K. Handique and M. A. Burns, *J. Micromech. Microeng.*, 2001, **11**, 548.
127 F. Sarrazin, L. Prat, N. Di Miceli, G. Cristobal, D. Link and D. Weitz, *Chem. Eng. Sci.*, 2007, **62**, 1042–1048.
128 J. T. Cabral and S. D. Hudson, *Lab Chip*, 2006, **6**, 427–436.
129 P. Paik, V. K. Pamula and R. B. Fair, *Lab Chip*, 2003, **3**, 253–259.
130 Y.-C. Tan, J. S. Fisher, A. I. Lee, V. Cristini and A. P. Lee, *Lab Chip*, 2004, **4**, 292–298.
131 D. Huh, J. H. Bahng, Y. Ling, H.-H. Wei, O. D. Kripfgans, J. B. Fowlkes, J. B. Grotberg and S. Takayama, *Anal. Chem.*, 2007, **79**, 1369–1376.
132 L. Wang, L. A. Flanagan, N. L. Jeon, E. Monuki and A. P. Lee, *Lab Chip*, 2007, **7**, 1114–1120.
133 S. K. Cho and Y. Zhao, *et al.*, *Lab Chip*, 2007, **7**, 490–498.
134 Y. Tan, Y. Ho and A. Lee, *Microfluid. Nanofluid.*, 2008, **4**, 343–348.
135 D. Huh, J. Bahng, Y. Ling, H. Wei, O. Kripfgans, J. Fowlkes, J. Grotberg and S. Takayama, *Anal. Chem.*, 2007, **79**, 1369–1376.
136 P. Nghe, E. Terriac, M. Schneider, Z. Z. Li, M. Cloitre, B. Abecassis and P. Tabeling, *Lab Chip*, 2011, **11**, 788–794.
137 C. L. Berli and M. L. Olivares, *J. Colloid Interface Sci.*, 2008, **320**, 582–589.
138 C. L. Berli, *Microfluid. Nanofluid.*, 2010, **8**, 197–207.
139 J. S. Hong and J. Cooper-White, *Korea-Aust. Rheol. J.*, 2009, **21**, 269–280.
140 P. Wilding, J. Pfahler, H. H. Bau, J. N. Zemel and L. J. Kricka, *Clin. Chem.*, 1994, **40**, 43–47.
141 C. Pipe and G. McKinley, *Mech. Res. Commun.*, 2009, **36**, 110–120.
142 S. Vagner and S. Patlazhan, *Langmuir*, 2019, **35**, 16388–16399.
143 A. Stroock, S. Dertinger, A. Ajdari, I. Mezic, H. Stone and G. Whitesides, *Science*, 2002, **295**, 647–651.
144 A. Stroock, S. Dertinger, G. Whitesides and A. Ajdari, *Anal. Chem.*, 2002, **74**, 5306–5312.
145 T. Nizkaya, E. Asmolov, J. Harting and O. Vinogradova, *Phys. Rev. Fluids*, 2020, **5**, 014201.

146 E. Asmolov, A. Dubov, T. Nizkaya, J. Harting and O. Vinogradova, *J. Fluid Mech.*, 2018, **840**, 613–630.
147 E. Asmolov, A. Dubov, T. Nizkaya, A. Kuehne and O. Vinogradova, *Lab Chip*, 2015, **15**, 2835–2841.
148 A. Rushton, G. Nteliopoulos, J. Shaw and R. Coombes, *Cancers*, 2021, **13**, 970.
149 E. Merrill, G. Cokelet, A. Britten and R. Wells, *Circ. Res.*, 1963, **13**, 48–55.
150 A. Semenov, M. Sorokina, M. Manoylov, P. Koshelev and R. Zhdanov, *Biomolecules*, 2020, **10**, 1448.
151 K. Loutherback, J. D'Silva, L. Liu, A. Wu, R. Austin and J. Sturm, *AIP Adv.*, 2012, **2**(4), 042107.
152 T. Rodrigues, R. Mota, L. Gales and L. Campo-Deaño, *J. Rheol.*, 2022, **66**, 761–774.
153 M. Brust, C. Schaefer, R. Doerr, L. Pan, M. Garcia, P. Arratia and C. Wagner, *Phys. Rev. Lett.*, 2013, **110**, 078305.
154 R. Larson, *Rheol. Acta*, 1992, **31**, 213–263.
155 S. Datta, A. Ardekani, P. Arratia, A. Beris, I. Bischofberger, G. McKinley, J. Eggers, J. López-Aguilar, S. Fielding and A. Frishman, *et al.*, *Phys. Rev. Fluids*, 2022, **7**, 080701.
156 H. Gao, J. Zhou, M. Naderi, Z. Peng and I. Papautsky, *Microsyst. Nanoeng.*, 2023, **9**, 73.
157 L. Helin, L. Thais and G. Mompean, *J. Non-Newtonian Fluid Mech.*, 2009, **156**, 84–94.
158 M. Moyers-Gonzalez and I. Frigaard, *J. Non-Newtonian Fluid Mech.*, 2020, **286**, 104440.
159 P. de Souza Mendes, M. Naccache, P. Varges and F. Marchesini, *J. Non-Newtonian Fluid Mech.*, 2007, **142**, 207–217.
160 H. Baniasadi, R. Abidnejad, M. Fazeli, J. Lipponen, J. Niskanen, E. Kontturi, J. Seppälä and O. Rojas, *Adv. Colloid Interface Sci.*, 2024, **324**, 103095.
161 S. De Smedt, B. Attaianese and R. Cardinaels, *Curr. Opin. Colloid Interface Sci.*, 2025, **75**, 101889.
162 M. Cooke, M. Riffe, M. Gomes, R. Domingues and J. Burdick, *Biofabrication*, 2025, **17**, 033001.
163 A. Rossi, T. Pescara, A. Gambelli, F. Gaggia, A. Asthana, Q. Perrier, G. Basta, M. Moretti, N. Senin, F. Rossi, G. Orlando and R. Calafiore, *Front. Bioeng. Biotechnol.*, 2024, **12**, 1393641.
164 H. Baniasadi, R. Ajdary, J. Trifol, O. Rojas and J. Seppälä, *Carbohydr. Polym.*, 2021, **266**, 118114.
165 C. Ma, Y. Wang, Z. Jiang, Z. Cao, H. Yu, G. Huang, Q. Wu, F. Ling, Z. Zhuang and H. Wang, *et al.*, *Chem. Eng. J.*, 2020, **399**, 125697.
166 A. Z. Nelson, B. Kundukad, W. K. Wong, S. A. Khan and P. S. Doyle, *Proc. Natl. Acad. Sci. U. S. A.*, 2020, **117**, 5671–5679.
167 E. Erfanian, R. Moaref, R. Ajdary, K. Tam, O. Rojas, M. Kamkar and U. Sundararaj, *Carbon*, 2023, **210**, 118037.
168 S. Marapureddy, P. Hivare, A. Sharma, J. Chakraborty, S. Ghosh, S. Gupta and P. Thareja, *Carbohydr. Polym.*, 2021, **269**, 118254.
169 C. Radeke, R. Pons, M. Mihajlovic, J. Knudsen, S. Butdayev, P. Kempen, C. Segeritz, T. Andresen, C. Pehmøller and T. Jensen, *et al.*, *ACS Appl. Mater. Interfaces*, 2023, **15**, 2564–2577.
170 J. van der Kolk, D. Tieman and M. Jalaal, *J. Fluid Mech.*, 2023, **958**, A34.
171 M. Jalaal, B. Stoeber and N. Balmforth, *J. Fluid Mech.*, 2021, **914**, A21.
172 L. Brunel, F. Christakopoulos, D. Kilian, B. Cai, S. Hull, D. Myung and S. Heilshorn, *Adv. Healthcare Mater.*, 2024, **13**, e2303325.
173 L. Brunel, S. Hull and S. Heilshorn, *Biofabrication*, 2022, **14**, 032001.
174 J. Karvinen and M. Kellomäki, *Eur. Polym. J.*, 2024, **209**, 112864.
175 J. Zhu and L. Cai, *Acta Biomater.*, 2023, **165**, 60–71.
176 L. Wang, X. Gong and W. Wen, *Microfluidics*, Springer, 2011, pp. 91–115.
177 L. Munteanu, A. Munteanu and M. Sedlacik, *Prog. Mater. Sci.*, 2024, 101421.
178 Y. Park and S. Choi, *Sensors*, 2024, **24**, 2842.
179 N. Kuznetsov, V. Kovaleva, S. Belousov and S. Chvalun, *Mater. Today Chem.*, 2022, **26**, 101066.
180 Y. Hong and W. Wen, *J. Intell. Mater. Syst. Struct.*, 2016, **27**, 866–871.
181 P. Sheng and W. Wen, *Annu. Rev. Fluid Mech.*, 2012, **44**, 143–174.
182 T. Hao, A. Kawai and F. Ikazaki, *Langmuir*, 2000, **16**, 3058–3066.
183 P. Chung, M. Jhon and H. Choi, *Phys. Fluids*, 2024, **36**, 083329.
184 P. Dhar, V. Saini, A. Chattopadhyay and D. Samanta, *Phys. Fluids*, 2021, **33**, 013101.
185 S. Ishii, H. Takahashi and Y. Sakai, *Smart Mater. Struct.*, 2024, **33**, 125017.
186 I. Chaudhary and M. Kaushal, *Soft Matter*, 2024, **20**, 3313–3321.
187 B. Qian, G. McKinley and A. Hosoi, *Soft Matter*, 2013, **9**, 2889–2898.
188 A. Bhattacharya and S. Chakraborty, *Langmuir*, 2025, **41**, 2347–2363.
189 E. Lauga, *Phys. Fluids*, 2014, **26**, 081902.
190 S. Godon, M. Kruusmaa and A. Ristolainen, *Front. Robot. AI*, 2023, 1113881.
191 D. Hewitt, *Rheol. Acta*, 2024, **63**, 673–688.
192 F. Nazari, K. Shoele and H. Mohammadigoushki, *Phys. Rev. Lett.*, 2023, **130**, 114002.
193 P. S. Eastham, H. Mohammadigoushki and K. Shoele, *J. Fluid Mech.*, 2022, **948**, A54.
194 D. R. Hewitt and N. J. Balmforth, *J. Fluid Mech.*, 2017, **828**, 33–56.
195 D. R. Hewitt and N. J. Balmforth, *J. Fluid Mech.*, 2022, **936**, A17.
196 B. Chan, N. J. Balmforth and A. E. Hosoi, *Phys. Fluids*, 2005, **17**, 113101.
197 R. H. Ewoldt, C. Clasen, A. E. Hosoi and G. H. McKinley, *Soft Matter*, 2007, **3**, 634–643.
198 C. Li, B. Qin, A. Gopinath, P. E. Arratia, B. Thomases and R. D. Guy, *J. R. Soc. Interface*, 2017, **14**, 20170289.

199 E. Lauga, M. P. Brenner and H. A. Stone, in *Microfluidics: The No-Slip Boundary Condition*, Springer, Berlin Heidelberg, 2007, pp. 1219–1240.
200 A. Y. Malkin and S. A. Patlazhan, *Adv. Colloid Interface Sci.*, 2018, **257**, 42–57.
201 S. G. Hatzikiriakos, *Prog. Polym. Sci.*, 2012, **37**, 624–643.
202 E. Younes, V. Bertola, C. Castelain and T. Burghelea, *Phys. Rev. Fluids*, 2020, **5**, 083303.
203 Y. Liu, D. Lorusso, D. W. Holdsworth, T. L. Poepping and J. R. de Bruyn, *J. Non-Newtonian Fluid Mech.*, 2018, **261**, 25–32.
204 J. Goyon, A. Colin, G. Ovarlez, A. Ajdari and L. Bocquet, *Nature*, 2008, **454**, 84–87.
205 J. Goyon, A. Colin and L. Bocquet, *Soft Matter*, 2010, **6**, 2668–2678.
206 V. Mansard and A. Colin, *Soft Matter*, 2012, **8**, 4025–4043.
207 R. Benzi, T. Divoux, C. Barentin, S. Manneville, M. Sbragaglia and F. Toschi, *EPL*, 2023, **141**, 56001.
208 D. Filippi, L. Derzsi, F. Nalin, A. Vezzani, D. Ferraro, A. Zaltron, G. Mistura and M. Pierno, *Adv. Mater. Technol.*, 2023, **8**, 2201748.
209 G. Guastella, D. Filippi, D. Ferraro, G. Mistura and M. Pierno, *Micromachines*, 2025, **16**, 335.
210 F. Pelusi, D. Filippi, L. Derzsi, M. Pierno and M. Sbragaglia, *Soft Matter*, 2024, **20**, 5203–5211.
211 S. Gupta and S. A. Vanapalli, *Phys. Fluids*, 2020, **32**, 012006.
212 E. F. Medina-Bañuelos, B. M. Marín-Santibáñez and J. Pérez-González, *J. Rheol.*, 2024, **68**, 361–379.
213 H. Rahmani, F. Larachi and S. M. Taghavi, *ACS Eng. Au*, 2024, **4**, 166–192.
214 A. Haase, J. Wood, L. Sprakel and R. Lammertink, *Phys. Rev. E*, 2017, **95**, 023105.
215 S. Patlazhan and S. Vagner, *Phys. Rev. E*, 2017, **96**, 013104.
216 P. K. Ray, D. Bouvier and D. T. Papageorgiou, *J. Non-Newtonian Fluid Mech.*, 2023, **319**, 105091.
217 O. Schnitzer and P. K. Ray, *Phys. Rev. Fluids*, 2024, **9**, L112201.
218 H. Rahmani and S. M. Taghavi, *J. Fluid Mech.*, 2022, **948**, A34.
219 H. Rahmani and S. M. Taghavi, *J. Non-Newtonian Fluid Mech.*, 2023, **315**, 105016.
220 H. Rahmani, H. Kumar, J. Greener and S. M. Taghavi, *Phys. Fluids*, 2023, **35**, 083107.
221 H. Rahmani and S. M. Taghavi, *J. Non-Newtonian Fluid Mech.*, 2024, **326**, 105203.
222 H. Rahmani and S. M. Taghavi, *J. Fluid Mech.*, 2024, **984**, A32.
223 A. Joulaei, H. Rahmani and S. Taghavi, *Phys. Rev. Fluids*, 2024, **9**, 123301.
224 A. Joulaei, H. Rahmani and S. Taghavi, *J. Non-Newtonian Fluid Mech.*, 2025, **341**, 105420.
225 A. Joulaei, A. Pal, H. Rahmani and S. Taghavi, *Phys. Fluids*, 2025, **37**, 053106.
226 A. Joulaei, H. Rahmani and S. Taghavi, *Lab Chip*, 2026, **26**, 1958–1979.
227 J. N. Wilking, T. E. Angelini, A. Seminara, M. P. Brenner and D. A. Weitz, *MRS Bull.*, 2011, **36**, 385–391.
228 A. A. Snowdon, S. P. Dennington, J. E. Longyear, J. A. Wharton and P. Stoodley, *Soft Matter*, 2023, **19**, 3675–3687.
229 M. J. Wells, *Ph.D. thesis*, University of Texas at Austin, Austin, Texas, USA, 2024.
230 R. Sudarsan, S. Ghosh, J. M. Stockie and H. J. Eberl, *Commun. Comput. Phys.*, 2016, **19**, 682–732.
231 M. U. Rahman, D. F. Fleming, I. Sinha, K. P. Rumbaugh, V. D. Gordon and G. F. Christopher, *Soft Matter*, 2021, **17**, 6225–6237.
232 L. Qi and G. F. Christopher, *Rheol. Acta*, 2021, **60**, 219–230.
233 G. Savorana, J. Słomka, R. Stocker, R. Rusconi and E. Secchi, *Soft Matter*, 2022, **18**, 3878–3890.
234 A. M. Hancock and S. S. Datta, *Biophys. J.*, 2024, **123**, 957–967.
235 D. L. Kurz, E. Secchi, F. J. Carrillo, I. C. Bourg, R. Stocker and J. Jimenez-Martinez, *Proc. Natl. Acad. Sci. U. S. A.*, 2022, **119**, e2122202119.
236 J. Greener, M. Parvinzadeh Gashti, A. Eslami, M. Zarabadi and S. Taghavi, *Biomicrofluidics*, 2016, **10**, 064107.
237 F. Paquet-Mercier, M. P. Gashti, J. Bellavance, S. M. Taghavi and J. Greener, *Lab Chip*, 2016, **16**, 4710–4717.
238 J. Greener, W. Y. Harvey, C. Gagné-Thivierge, S. Fakhari, S. M. Taghavi, J. Barbeau and S. J. Charette, *Phys. Fluids*, 2022, **34**, 021902.
239 L. Mohan, M. Cloitre and R. T. Bonnecaze, *J. Rheol.*, 2014, **58**, 1465–1482.
240 A. Mutneja and K. S. Schweizer, *J. Rheol.*, 2025, **69**, 297–314.
241 A. Ahuja, A. Potanin and Y. Joshi, *Adv. Colloid Interface Sci.*, 2020, **282**, 102179.
242 V. Vitali, G. Nava, A. Corno, M. Pezzotti, F. Bragheri, P. Paiè, R. Osellame, M. A. Ortenzi, I. Cristiani and P. Minzioni, *et al.*, *Soft Matter*, 2021, **17**, 3105–3112.
243 S. Meeker, R. Bonnecaze and M. Cloitre, *Phys. Rev. Lett.*, 2004, **92**, 198302–198302.
244 M. Cloitre and R. Bonnecaze, *Rheol. Acta*, 2017, **56**, 283–305.
245 B. D. Jofore, P. Erni, G. Vleminckx, P. Moldenaers and C. Clasen, *Rheol. Acta*, 2015, **54**, 581–600.
246 T. Divoux, C. Barentin and S. Manneville, *Soft Matter*, 2011, **7**, 8409–8418.
247 Y. M. Joshi and G. Petekidis, *Rheol. Acta*, 2018, **57**, 521–549.
248 G. Vleminckx and C. Clasen, *Curr. Opin. Colloid Interface Sci.*, 2014, **19**, 503–513.
249 F. Loosli, M. Najm, R. Chan, E. Oikonomou, A. Grados, M. Receveur and J.-F. Berret, *ChemPhysChem*, 2016, **17**, 4134–4143.
250 S. Choi, S. Steltenkamp, J. Zasadzinski and T. Squires, *Nat. Commun.*, 2011, **2**, 312.
251 B. Géraud, L. Jørgensen, C. Ybert, H. Delanoë-Ayari and C. Barentin, *Eur. Phys. J. E: Soft Matter Biol. Phys.*, 2017, **40**, 5.
252 Z. Jaworski, T. Spychaj, A. Story and G. Story, *Rev. Chem. Eng.*, 2022, **38**, 881–919.
253 A. Nicolas, E. E. Ferrero, K. Martens and J.-L. Barrat, *Rev. Mod. Phys.*, 2018, **90**, 045006.
254 L. Bocquet, A. Colin and A. Ajdari, *Phys. Rev. Lett.*, 2009, **103**, 036001.

255 E. Stiakakis, A. Wilk, J. Kohlbrecher, D. Vlassopoulos and G. Petekidis, *Phys. Rev. E: Stat., Nonlinear, Soft Matter Phys.*, 2010, **81**, 020402.
256 J. Song, M. Caggioni, T. M. Squires, J. F. Gilchrist, S. W. Prescott and P. T. Spicer, *Rheol. Acta*, 2019, **58**, 217–229.
257 A. Penneron, T. Brunet and D. Baresch, *Appl. Phys. Lett.*, 2025, **126**, 084104.
258 B. Saint-Michel and V. Garbin, *Soft Matter*, 2020, **16**, 10405–10418.
259 J. B. Estrada, C. Barajas, D. L. Henann, E. Johnsen and C. Franck, *J. Mech. Phys. Solids*, 2018, **112**, 291–317.
260 T. Gibaud, N. Dagès, P. Lidon, G. Jung, L. C. Ahouré, M. Sztucki, A. Poulesquen, N. Hengl, F. Pignon and S. Manneville, *Phys. Rev. X*, 2020, **10**, 011028.
261 S. Iwata, Y. Yamada, T. Takashima and H. Mori, *J. Non-Newtonian Fluid Mech.*, 2008, **151**, 30–37.
262 S. J. Haward, *Biomicrofluidics*, 2016, **10**, 043401.
263 S. Varchanis, G. Makrigiorgos, Y. Dimakopoulos and J. Tsamopoulos, *Proc. Natl. Acad. Sci. U. S. A.*, 2020, **117**, 12611–12617.
264 A. Geffrault, H. Bessaies-Bey, N. Roussel and P. Coussot, *J. Rheol.*, 2021, **65**, 887–901.
265 B. Laborie, F. Rouyer, D. E. Angelescu, E. Lorenceau, D. Bonn and H. Kellay, *Phys. Rev. Lett.*, 2015, **114**, 204501.
266 A. Schwab, R. Levato, M. D'Este, S. Piluso, D. Eglin and J. Malda, *Chem. Rev.*, 2020, **120**, 11028–11055.
267 I. Sudreau, M. Auxois, M. Servel, É. Lécolier, S. Manneville and T. Divoux, *Phys. Rev. Mater.*, 2022, **6**, L042601.
268 Y. Chen, Q. Zhang, S. Ramakrishnan and R. Leheny, *J. Chem. Phys.*, 2023, **158**, 024906.
269 K. Kamani, Y. Shim, J. Griebler, S. Narayanan, Q. Zhang, R. Leheny, J. Harden, A. Deptula, R. Espinosa-Marzal and S. Rogers, *Soft Matter*, 2025, **21**, 750–759.
270 P. Edera, M. Bantawa, S. Aime, R. Bonnecaze and M. Cloitre, *Phys. Rev. X*, 2025, **15**, 011043.
271 T. Waigh, *Rep. Prog. Phys.*, 2005, **68**, 685.
272 D. Weihs, T. Mason and M. Teitell, *Biophys. J.*, 2006, **91**, 4296–4305.
273 T. Squires and T. Mason, *Annu. Rev. Fluid Mech.*, 2010, **42**, 413–438.
274 Z. Rehman, U. Khalid, K. Farooq and H. Mujtaba, *Int. J. Geo-Eng.*, 2018, **9**, 21.
275 K. Yang and W. Yu, *J. Rheol.*, 2017, **61**, 627–641.
276 P. Cicuta and A. Donald, *Soft Matter*, 2007, **3**, 1449–1455.
277 F. MacKintosh and C. Schmidt, *Curr. Opin. Colloid Interface Sci.*, 1999, **4**, 300–307.
278 T. Waigh, *Rep. Prog. Phys.*, 2016, **79**, 074601.
279 A. Lindner, P. Coussot and D. Bonn, *Phys. Rev. Lett.*, 2000, **85**, 314.
280 A. Eslami and S. Taghavi, *J. Non-Newtonian Fluid Mech.*, 2017, **243**, 79–94.
281 J. V. Fontana, S. A. Lira and J. A. Miranda, *Phys. Rev. E: Stat., Nonlinear, Soft Matter Phys.*, 2013, **87**, 013016.
282 J. R. de Bruyn, P. Habdas and S. Kim, *Phys. Rev. E: Stat., Nonlinear, Soft Matter Phys.*, 2002, **66**, 031504.
283 A. Eslami and S. Taghavi, *Phys. Rev. E*, 2020, **102**, 023105.
284 A. Eslami, R. Basak and S. M. Taghavi, *Ind. Eng. Chem. Res.*, 2020, **59**, 4119–4133.
285 A. Eslami and S. Taghavi, *J. Non-Newtonian Fluid Mech.*, 2019, **264**, 25–47.
286 B. Ebrahimi, P. Mostaghimi, H. Gholamian and K. Sadeghy, *J. Eng. Math.*, 2016, **97**, 161–176.
287 A. Pouplard and P. A. Tsai, *Sci. Rep.*, 2024, **14**, 2338.
288 T. Divoux, A. Shukla, B. Marsit, Y. Kaloga and I. Bischofberger, *Phys. Rev. Lett.*, 2020, **124**, 248006.
289 V. Parmar, D. Saha and R. Bandyopadhyay, *JCIS Open*, 2022, **6**, 100047.
290 V. Parmar and R. Bandyopadhyay, *JCIS Open*, 2023, **10**, 100084.
291 V. Parmar and R. Bandyopadhyay, *EPL*, 2024, **145**, 47001.
292 T. Tu, Y. Shen, S. Lim and Y. Wang, *Front. Bioeng. Biotechnol.*, 2022, **10**, 877480.
293 E. Delannoy, G. Tellier, J. Cholet, A. Leroy, A. Treizebré and F. Soncin, *Biomedicines*, 2022, **10**, 797.
294 L. Bischel, S. Lee and D. Beebe, *J. Lab. Autom.*, 2012, **17**, 96–103.
295 G. M. Homsy, *Annu. Rev. Fluid Mech.*, 1987, **19**, 271–311.
296 A. Lindner, P. Coussot and D. Bonn, *Phys. Rev. Lett.*, 2000, **85**, 314–317.
297 A. Dufresne, T. Ball and N. Balmforth, *J. Non-Newtonian Fluid Mech.*, 2023, **312**, 104970.
298 D. Pritchard, *J. Non-Newtonian Fluid Mech.*, 2006, **135**, 117–127.

